Inorganic Chemistry
Cite This: Inorg. Chem. 2019, 58, 15726−15740
Article
pubs.acs.org/IC

Coligand Effects on the Field-Induced Double Slow Magnetic Relaxation in Six-Coordinate Cobalt(II) Single-Ion Magnets (SIMs) with Positive Magnetic Anisotropy

Julia Vallejo,[†] Marta Viciano-Chumillas,[†] Francisco Lloret,[†] Miguel Julve,[†] Isabel Castro,[†] J. Krzystek,*[,‡] Mykhaylo Ozerov,[‡] Donatella Armentano,[§] Giovanni De Munno,*[,§] and Joan Cano*[,†]

[†]Institut de Ciència Molecular (ICMol) and Departament de Química Inorgànica, Universitat de València, 46980 Paterna, València
[‡]National High Magnetic Field Laboratory, Florida State University, Tallahassee, Florida 32310, United States
[§]Dipartamento di Chimica e Tecnologie Chimiche, Università della Calabria, 87036 Rende, Cosenza Italy

Supporting Information

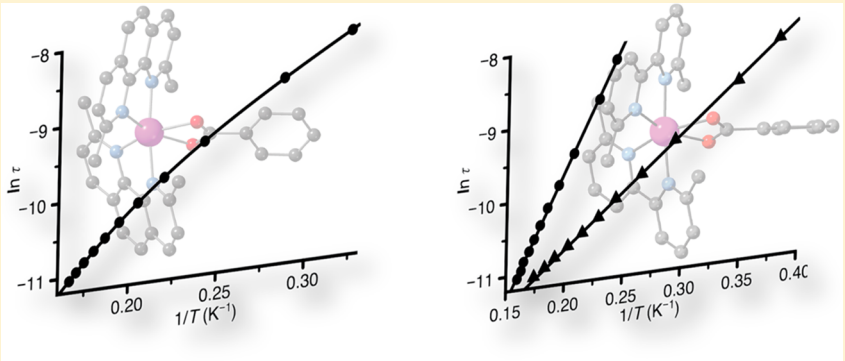

ABSTRACT: Two mononuclear cobalt(II) compounds of formula $[Co(dmphen)_2(OOCPh)]ClO_4 \cdot 1/2H_2O \cdot 1/2CH_3OH$ (**1**) and $[Co(dmbipy)_2(OOCPh)]ClO_4$ (**2**) (dmphen = 2,9-dimethyl-1,10-phenanthroline, dmbipy = 6,6′-dimethyl-2,2′-bipyridine and HOOCPh = benzoic acid) are prepared and magnetostructurally investigated. Each cobalt(II) ion is six-coordinate with a distorted octahedral CoN_4O_2 environment. The complex cations are interlinked leading to supramolecular chains (**1**) and pairs (**2**) that grow along the crystallographic *c*-axis with racemic mixtures of (Δ,Λ)-Co units. FIRMS allowed us to directly measure the zero-field splitting between the two lowest Kramers doublets, which led to axial anisotropy values of 58.3 $cm^{-1} \leq D <$ 60.7 cm^{-1} (**1**) and 63.8 $cm^{-1} \leq D <$ 64.1 cm^{-1} (**2**). HFEPR spectra of polycrystalline samples of **1** and **2** at low temperatures confirm the positive sign of *D* and provide an estimate of the *E*/*D* quotient [0.147/0.187 (**1**) and 0.052 (**2**)]. Detailed ac and dc magnetic studies reveal that **1** and **2** are new examples of field-induced single-ion magnets (SIMs) with small transversal anisotropy. CASSCF/NEVPT2 calculations support these results. Two Orbach processes or one Orbach plus a direct relaxation mechanism provide similar agreements with the nonlinear experimental Arrhenius plots at H_{dc} = 500 and 2500 G for **1**. Two independent relaxation processes occur in **2**, but in contrast to **1**, an observed linear dependence of ln(τ) vs 1/*T* substantiates Orbach processes against the most widely proposed Raman and direct mechanisms. The analysis of each relaxation process in **2** provided values for E_a and τ_0 that are very close to those found for **1**, validating the predominant role of the Orbach relaxations in both compounds and, probably, also in other cobalt(II) SIMs. A mechanism based on a spin-phonon coupling is proposed to account for the SIM behavior in **1** and **2** with any Raman or direct processes being discarded.

INTRODUCTION

Single-molecule magnets (SMMs) have attracted much attention in the recent past because of the quantum properties associated with their ability to act as magnets exhibiting a remnant magnetic moment from a purely molecular origin.[1] During several decades, these properties were related to a high spin moment (*S*) and a large axial magnetic anisotropy (*D*). Consequently, the efforts were focused on increasing these parameters by using the chemical skills for the synthesis of polynuclear compounds.[2,3] However, the common misalignment of the individual zero-field splitting (*zfs*) tensors results in a decrease, a cancellation, or a change of the sign of the resulting axial component in the molecule. This feature would decrease the performance of the desired SMM or even nullify it.[4,5] Thus, the control of the magnetic anisotropy through the molecular design has become a challenge.

Received: June 10, 2019
Published: November 18, 2019

Downloaded via FLORIDA STATE UNIV on January 7, 2020 at 02:28:03 (UTC).
See https://pubs.acs.org/sharingguidelines for options on how to legitimately share published articles.

ACS Publications © 2019 American Chemical Society

DOI: 10.1021/acs.inorgchem.9b01719
Inorg. Chem. 2019, 58, 15726−15740

For the above reason, given that the *zfs* arises from a significant orbital contribution, new strategies have emerged dealing with the use of lanthanide and actinide ions.[6−8] Another strategy is based on broadening the physical concepts developed for the SMMs to less sophisticated mononuclear complexes that exhibit slow magnetic relaxation, commonly known as single-ion magnets (SIMs). The reduced size of these systems makes easier the control of the above-mentioned parameters. The first examples of this research line involved lanthanide and actinide cations with large magnetic anisotropy.[9,10] Amazingly enough, some years later, SIMs from the first-row transition metals with a nonzero *zfs* were also described.[11−18]

Among all reported SIMs based on 3d metal centers, the most popular are those with cobalt(II) ions because of their first order spin−orbit coupling (SOC) in an octahedral surrounding.[16,19−26] However, cobalt(II) compounds with different geometries, such as tetrahedral or pseudotetrahedral,[13,27−41] square-pyramidal,[14,42,43] trigonal bipyramidal,[42,44,45] octahedral,[16,20−23,26,46−48] trigonal prism,[20,21,49] pentagonal bipyramidal,[50,51] etc., can also exhibit SIM behavior. The primary concern in such compounds derives from the unpredictable sign of the anisotropy, that can be either positive (easy-plane) or negative (easy-axis). In the past, the most common thinking was that an easy-axis anisotropy was required to exhibit the SIM behavior, being right for those systems with a second order SOC.[15] However, mononuclear cobalt(II) complexes with positive *D* coming from a first order SOC also present this particular behavior, though governed by a different mechanism. In these systems with large positive *D* values, there is no barrier for the spin inversion, and the activation energies do not relate to the values of the *zfs* parameters. Thus, a very carefully thought-out design of new complexes is necessary to elucidate the physics that is behind this phenomenon.

In a previous paper, some of us reported the first example of a six-coordinated mononuclear cobalt(II) compound with SIM properties,[16] where two N-bonded thiocyanate groups (NCS^-) and two chelating dmphen (dmphen = 2,9-dimethyl-1,10-phenanthroline) molecules define the coordination sphere of the Co(II) ion. Its particular magnetic properties arise from a large positive anisotropy (*D*) and a considerable rhombicity (*E*) induced by a distortion imposed by the two sterically hindered dmphen ligands. Herein, we extend our studies to the effects of the ligands on the cobalt geometry and magnetic properties. With this idea in mind, the thiocyanate ligands are substituted by anionic benzoate groups expecting that its potential chelating nature and its small bite angle would induce significant geometrical constraints at the metal center. In this paper, we focus on two new six-coordinate heteroleptic cobalt(II) compounds of formula $[Co(dmphen)_2(OOCPh)]ClO_4{\cdot}1/2H_2O{\cdot}1/2CH_3OH$ (**1**) and $[Codmbipy)_2(OOCPh)]ClO_4$ (**2**), (dmbipy = 6,6′-dimethyl-2,2′-bipyridine and HOOCPh = benzoic acid) which slightly differ in the N-donor ligand (see Figure 1). Their synthesis, X-ray structure, and cryomagnetic investigation together with a comparison of their dynamic magnetic behaviors are presented here. From the differences in the dynamic behavior of **1** and **2**, it was possible to conclude that a relaxation via either Raman or direct processes should not be involved in octahedral cobalt(II) complexes, with the more promising candidate being a spin-phonon coupling the Orbach mechanism associated with a spin-phonon coupling being the more promising candidate.

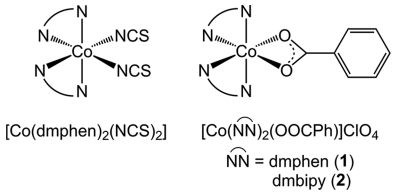

Figure 1. Six-coordinate cobalt(II) SIMs: (left) previously reported[16] and (right) presented herein.

EXPERIMENTAL SECTION

Materials. All chemicals were of reagent grade quality. They were purchased from commercial sources and used as received.

Caution! Perchlorate salts with organic ligands are potentially explosive. We work on a mmol scale and any heating is avoided.

Synthesis of $[Co(dmphen)_2(OOCPh)]ClO_4{\cdot}1/2H_2O{\cdot}1/2CH_3OH$ (1). A methanolic solution of dmphen (0.104 g, 0.5 mmol) was added to an aqueous solution (5 mL) of $Co(ClO_4)_2{\cdot}6H_2O$ (0.09 g, 0.25 mmol) under continuous stirring. Finally, a water solution of sodium benzoate (0.036 g, 0.25 mmol) was poured into the resulting mixture. X-ray quality pink cubic crystals were grown after a few days by slow evaporation at room temperature. The crystals were collected by filtration and air-dried. Yield: 78% (0.28 g). Anal. Calcd for $C_{35.5}H_{32}ClCoN_4O_7$ (**1**): C, 59.13; H, 4.47; N, 7.77. Found: C, 58.96; H, 4.33; N, 7.61%. IR (ν_{max}/cm^{-1}, KBr): 1594 [$\nu_{as}(COO^-)$], 1420 [$\nu_s(COO^-)$], 1090 [$\nu_3(ClO_4^-)$], 937 [$\nu_1(ClO_4^-)$], 622 [$\nu_4(ClO_4^-)$].

Synthesis of $[Co(dmbipy)_2(OOCPh)]ClO_4$ (2). Compound **2** was synthesized following the same procedure of **1**, but using dmbipy instead of dmphen. Violet chunky crystals were grown by slow evaporation under ambient conditions. They were collected by filtration and dried on filter paper. Yield: 92% (0.30 g). Anal. Calcd for $C_{31}H_{29}ClCoN_4O_6$ (**2**): C, 57.46; H, 4.51; N, 8.65. Found: C, 57.95; H, 4.63; N, 8.79%. IR (ν_{max}/cm^{-1}, KBr): 1600 [$\nu_{as}(COO^-)$], 1427 [$\nu_s(COO^-)$], 1086 [$\nu_3(ClO_4^-)$], 929 [$\nu_1(ClO_4^-)$], 623 [$\nu_4(ClO_4^-)$].

Physical Measurements. Infrared spectra (4000−400 cm^{-1}) were recorded on a Nicolet 5700 spectrophotometer as KBr pellets. Elemental analyses (C, H, N) were performed at the Servei Central de Suport a la Investigació (SCSIE) from the Universitat de València (Spain). Variable-temperature (2−300 K) direct current (dc) magnetic susceptibility measurements on crushed crystals of **1** and **2** under applied fields of 0.25 ($T < 30$ K) and 5.0 kG ($T \geq 30$ K) and variable-field (0−5 T) magnetization measurements in the temperature range 2.0−10.0 K were carried out with a Quantum Design SQUID magnetometer. Variable-temperature (2.0−10.0 K) alternating current (ac) magnetic susceptibility measurements at frequencies in the range 0.6−10.0 kHz under ±5.0 G oscillating field and different applied static dc fields in the range 0−2.5 kG were performed with a Quantum Design Physical Property Measurement System (PPMS). Data were corrected for the diamagnetism of the constituent atoms and the sample holder. The crushed samples of **1** and **2** were restrained with *n*-eicosane to prevent any displacement due to their significant magnetic anisotropy. Far-infrared magnetic spectroscopy (FIRMS, also known as frequency-domain magnetic resonance spectroscopy) experiments were performed at the National High Magnetic Field Laboratory using a Bruker Vertex 80v FT-IR spectrometer coupled with a 17 T vertical-bore superconducting magnet in a Voigt configuration (light propagation perpendicular to the external magnetic field). The experimental setup employs broadband terahertz radiation emitted by a Hg arc lamp. The radiation transmitted through the sample was detected by a composite silicon bolometer (Infrared Laboratories) mounted at the end of the quasioptical transmission line. Both sample and bolometer were cooled by a low-pressure helium gas to the temperature of 4.6 K. The intensity spectra of the microcrystalline powder sample (∼7 mg) bonded by *n*-eicosane were measured in the spectral region between 14 and 730 cm^{-1} (0.42−22 THz) with a resolution of 0.3 cm^{-1} (9

DOI: 10.1021/acs.inorgchem.9b01719
Inorg. Chem. 2019, 58, 15726−15740

GHz). To discern the magnetic absorptions, the spectra were divided by the reference spectrum, which is the average spectrum for all magnetic fields. Such normalized transmittance spectra are only sensitive to transmission changes induced by the magnetic field and therefore obscure nonmagnetic contribution to the intensity spectrum. All data analysis routine was implemented by in-house written MATLAB code and the EPR simulation software package EasySpin.[52] High-frequency and -field EPR (HFEPR) spectra of **1** and **2** were recorded at 4.5 K on polycrystalline samples (20−25 mg) using a homodyne spectrometer at the EMR facility associated with a 15/17-T superconducting magnet and a frequency range from 52 to 426 GHz. Detection was provided with an InSb hot electron bolometer (QMC Ltd., Cardiff, UK). The magnetic field was modulated at 50 kHz for detection purposes. A Stanford Research Systems SR830 lock-in amplifier converted the modulated signal to dc voltage. The single-frequency spectra as well as their dependencies on frequency were simulated with the SPIN software from A. Ozarowski.

Computational Details. Calculations based on a second-order N-electron valence state perturbation theory (CASSCF/NEVPT2) applied on the wave function, which was previously obtained from complete active space (CAS) calculation, were performed on the structurally characterized mononuclear complexes **1** and **2** aiming to evaluate the parameters that determine the axial (D) and rhombic (E) *zfs* in them.[53−55] These mononuclear species keep the experimental dispositions of the ligands around the metal. The calculations were carried out with version 4.0 of the ORCA program[56] using the TZVP basis set proposed by Ahlrichs[57,58] and the auxiliary TZV/C Coulomb fitting basis sets.[59,60] The spin−orbit coupling contributions to *zfs* from 10 quartet and 20 doublet excited states generated from an active space with seven electrons in five d-orbitals were included from an effective Hamiltonian. The g-tensors were calculated for the ground Kramer's pair using Multireference Configuration Interaction (MRCI) wave functions with a first-order perturbation theory on the SOC matrix.[61]

DFT calculations were carried out through the Gaussian 09 package in order to estimate the magnitude of the intermolecular magnetic couplings.[62] These calculations were performed with the CAM-B3LYP hybrid functional,[63−66] the quadratic convergence approach, and a guess function generated with the fragment tool of the same program. Triple-ζ and double-ζ all-electron basis sets proposed by Ahlrichs et al. were employed for metal and nonmetal atoms, respectively.[57,58] The study was done using models including two neighboring cobalt(II) complexes in their experimental geometries. The magnetic coupling states were obtained from the relative energies of the broken-symmetry (BS) singlet spin state from the high-spin state with parallel local spin moments. More details about the use of the broken-symmetry approach to evaluate the magnetic coupling constants can be found in the literature.[67−69] A polarizable continuum model (PCM) was introduced in the calculations with the parameters corresponding to the acetonitrile.[70] The optimizations of the molecular geometry on the mononuclear cobalt(II) complexes in **1** and **2** were done starting from their experimental geometries and using the CAM-B3LYP functional such as it is implemented in Gaussian09 packages.[62] To improve the goodness of the calculated analytical vibrational frequencies, restricted conditions were imposed in the self-consistent convergence of the wave function and the evaluation of the bielectronic integrals (very tight and ultrafine, respectively) for the optimization of the geometry and the evaluation of the vibrational modes.

X-ray Crystallography. Single-crystal X-ray diffraction data of **1** and **2** were collected at 100(2) and 296(2) K, respectively, on a Bruker-Nonius KappaCCD diffractometer by using graphite-monochromated Mo Kα radiation (λ = 0.71073 Å). All calculations for data reduction, structure solution, and refinement were done through the *SAINT*[71] and *SADABS*[72] programs. The structures of **1** and **2** were solved by direct methods and subsequently completed by Fourier recycling using the version 2018/3 of the *SHELXTL* software package.[73] All non-hydrogen atoms were refined with anisotropic displacement parameters. Positional disorder on perchlorate anions has been modeled, and oxygen atoms have been refined on two sets of positions in both **1** and **2** with occupancy factors of 0.9 and 0.1 (**1**) and 0.4 and 0.6 (**2**). All hydrogen atoms were placed at calculated positions, and they were refined riding on the parent atoms. Geometrical calculations and molecular graphics were performed with *PLATON*[74] and *CRYSTALMAKER*[75] programs. Crystallographic data for the structures reported in this article have been deposited with the Cambridge Crystallographic Data Centre as supplementary publication no. CCDC-1914219 (**1**) and CCDC-1914220 (**2**). The comments for the alerts are described in the CIFs using the validation reply form (vrf). Copies of the data can be obtained free of charge on application to CCDC, 12 Union Road, Cambridge CB21EZ, UK (fax: (+44) 1223-336-033; e-mail: deposit@ccdc.cam.ac.uk). Crystallographic data and refinement statistics for **1** and **2** are given in Table 1 whereas main bond lengths and angles for them are listed in Table 2.

Table 1. Crystal Data and Structure Refinement for 1 and 2

	1	2
Formula	$C_{71}H_{64}Cl_2Co_2N_8O_{14}$	$C_{31}H_{29}ClCoN_4O_6$
Formula weight	1442.06	647.96
Crystal system	triclinic	Monoclinic
Space group	$P\bar{1}$	$P2_1/c$
a (Å)	10.95031(14)	12.9365(4)
b (Å)	13.5487(17)	18.5740(6)
c (Å)	22.989(3)	13.9168(5)
α (deg)	107.118(5)	90
β (deg)	91.241(5)	115.974(1)
γ (deg)	98.314(5)	90
V (Å^3)	3217.9(7)	3006.20(17)
Z	2	4
ρ_{calc} (g cm^{-3})	1.488	1.432
μ (mm^{-1})	0.674	0.710
T (K)	100	296
F(000)	1492	1340
Reflections collected	82803	19835
Independent reflections (R_{int})	12925 (0.028)	2671 (0.027)
Observed reflections [$I > 2\sigma(I)$]	11578	2419
R_1[a] [$I > 2\sigma(I)$]	0.0353	0.0333
wR_2[b] [$I > 2\sigma(I)$] (all)	0.0977 (0.1019)	0.0785 (0.0818)
Goodness-of-fit on F^2	1.002	1.068
Largest diff. peak/hole [e Å^{-3}]	1.035/−1.079	0.320/−0.241

[a] $R_1 = \sum(|F_0| - |F_c|)/\sum|F_0|$. [b] $wR_2 = [\sum w(F_0^2 - F_c^2)^2/\sum w(F_0^2)^2]^{1/2}$.

X-ray powder diffraction (XRPD) measurements on **1** and **2** were performed on a Panalytical Empyrean X-ray diffractometer by using Cu Kα radiation (λ = 1.5418 Å), in which the X-ray tube was operated at 40 kV and 30 mA ranging from 5 to 40°.

RESULTS AND DISCUSSION

Synthesis and General Characterization. Compounds **1** and **2** were prepared in good yields by the reaction between the stoichiometric amounts of cobalt(II) perchlorate hexahydrate, the corresponding methyl-substituted α-diimine ligand [dmphen (**1**) and dmbipy (**2**)], and sodium benzoate in a H_2O:MeOH mixture as solvent. To confirm the phase purity of the synthesized complexes, their XRPD spectra were recorded. As can be seen in Figures S1 (**1**) and S2 (**2**) (see Supporting Information), the XRPD patterns measured for polycrystalline samples of **1** and **2** are in good agreement with those simulated from the respective single-crystal X-ray data, demonstrating that the crystal structures are truly representative of the bulk materials. The occurrence of two strong absorption peaks at 1594/1420 (**1**) and at 1600/1427 cm^{-1} (**2**) in the infrared spectra of **1** and **2** (Figures S3 and S4), which correspond to

DOI: 10.1021/acs.inorgchem.9b01719
Inorg. Chem. 2019, 58, 15726−15740

Table 2. Selected Bond Distances and Angles for 1 and 2

	1	2
Co1−N1	2.1463(16)	2.180(3)
Co1−N2	2.1305(16)	2.135(3)
Co1−N3	2.1188(16)	2.128(3)
Co1−N4	2.1726(16)	2.175(3)
Co1−O1	2.2155(13)	2.173(2)
Co1−O2	2.1632(14)	2.160(2)
Co2−N5	2.1301(16)	
Co2−N6	2.1692(17)	
Co2−N7	2.1260(16)	
Co2−N8	2.1209(16)	
Co2−O3	2.2613(14)	
Co2−O4	2.1541(13)	
N1−Co1−N2	79.32(6)	77.6(1)
N1−Co1−N3	104.20(6)	105.8(1)
N1−Co1−N4	172.64(6)	105.8(1)
N2−Co1−N3	108.63(6)	105.2(2)
N2−Co1−N4	106.60(6)	175.1(1)
N3−Co1−N4	78.33(6)	77.6(1)
O1−Co1−O2	60.56(5)	60.8(1)
O1−Co1−N1	93.82(6)	97.3(1)
O1−Co1−N2	157.01(6)	97.26(11)
O1−Co1−N3	94.30(6)	158.81(11)
O1−Co1−N4	79.04(6)	94.42(11)
N5−Co2−N6	78.43(6)	
N5−Co2−N7	100.32(6)	
N5−Co2−N8	108.85(6)	
N6−Co2−N7	172.85(6)	
N6−Co2−N8	106.77(6)	
N7−Co2−N8	80.33(6)	
O3−Co2−O4	59.89(5)	
O3−Co2−N5	158.67(5)	
O3−Co2−N6	96.73(6)	
O3−Co2−N7	81.87(6)	
O3−Co2−N8	92.46(6)	

the $\nu_{as}(COO^-)/\nu_s(COO^-)$ stretching vibrations of the carboxylate group with Δ = 174 (**1**) and 173 cm^{-1} (**2**) [to be compared with Δ = 142 cm^{-1} for sodium benzoate, with Δ being defined as $\nu_{as}(COO^-) - \nu_s(CCO^-)$], suggests the coordination of the benzoate in them.[76,77] The set of strong (ν_3), weak (ν_1), and medium (ν_4) intensity peaks at 1090, 937, and 622 (**1**) and 1086, 929, and 623 cm^{-1} (**2**) is indicative of the occurrence of ionic perchlorate in **1** and **2**.[78] Finally, the C−H stretching modes of the aromatic and aliphatic C−H groups in the high-frequency range 2900−3100 cm^{-1} (**1** and **2**) as well as the δ(C−H) vibrations of the aromatic rings [732 and 683 cm^{-1} (**1**) and 794 and 721 cm^{-1} (**2**)] are a diagnostic of the presence of the methyl-substituted α-diimines in these compounds. All these spectroscopic features for **1** and **2** were confirmed by their X-ray structures (see below).

Description of the Structures of 1 and 2. Compounds **1** and **2** crystallize in the triclinic $P\bar{1}$ and the monoclinic $P2_1/c$ space groups, respectively. Their crystal structures consist of mononuclear complex cations $[Co(dmphen)_2(OOCPh)]^+$ (**1**) and $[Co(dmbipy)_2(OOCPh)]^+$ (**2**) (Figure 2), perchlorate anions (**1** and **2**), and water and methanol molecules of crystallization (**1**). Although two crystallographically distinct cobalt atoms [Co1/Co2 (Figure 2, top)] exist in **1**, they have the same surrounding with very close bond lengths and angles (see Table 2).

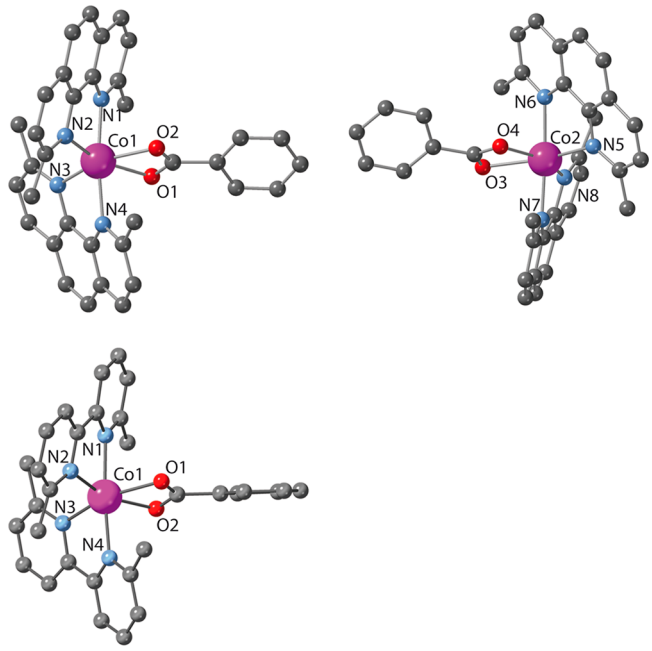

Figure 2. View of the mononuclear complex cation $[Co1/Co2(dmphen)_2(OOCPh)]^+$ (**1**, top) and $[Co(dmbipy)_2(OOCPh)]^+$ (**2**, bottom). Hydrogen atoms are omitted for clarity. Color code: magenta (cobalt), blue (nitrogen), red (oxygen), and gray (carbon).

The cobalt environment in both compounds complies with a highly distorted CoN_4O_2 octahedron, wherein the two oxygen atoms of the carboxylate ligand and two nitrogen atoms from two different α-diimine ligands define the equatorial plane, with the metal ion being slightly displaced from the mean N_2O_2 equatorial plane [0.003 (Co1) and 0.010 Å (Co2) in **1** and 0.014 Å (Co1) in **2**]. The two remaining α-diimine nitrogen atoms occupy the axial positions. The values of the cobalt-to-nitrogen bond lengths cover the ranges 2.12−2.17 (**1**) and 2.13−2.19 Å (**2**). The bidentate coordination of the carboxylate group is somewhat more asymmetric in **1** than in **2** [Co−O = 2.16 and 2.22 (at Co1) and 2.15 and 2.26 Å (at Co2) in **1** and 2.16 and 2.17 Å (at Co1) in **2**]. The values of the angle subtended at each cobalt atom by the chelating dmphen [values in the range 78.33(6)−80.33(6)°] and dmbipy [77.5(2) and 77.6(2)°] ligands deviate from the angle of an ideal octahedron (90°). This deviation is even greater for the bidentate carboxylate, with the values of the O−Co−O bite angle being 60.56 (Co1) and 59.92° (Co2) in **1** and 59.89° (Co1) in **2**. They are in agreement with those from other chelating carboxylate groups reported in the literature.[79,80] These angles are the primary source of the distortion of the coordination sphere that indirectly leads to deviations of the planarity of the two pyridyl rings of the dmphen and dmbpy ligands [dihedral angles of 1.39 and 8.32°, and 7.59 and 6.33° (**1**) and 7.03 and 8.52° (**2**)] and also of the N_2O_2 equatorial plane [CoO_2/CoN_2 dihedral angles = 1.01 and 2.92° (**1**) and 7.09° (**2**)]. On the other hand, the phenyl ring and the carboxylate group from the benzoate ligand are not coplanar [18.80 and 32.27° (**1**) and 24.25° (**2**)].

The distortion degree for both compounds was calculated with the continuous shape measure theory through the SHAPE software,[81] which places a structure on the path that draws the transformation between two ideal polyhedra. This methodology uses a parameter to provide a measure of the deviation

DOI: 10.1021/acs.inorgchem.9b01719
Inorg. Chem. 2019, 58, 15726−15740

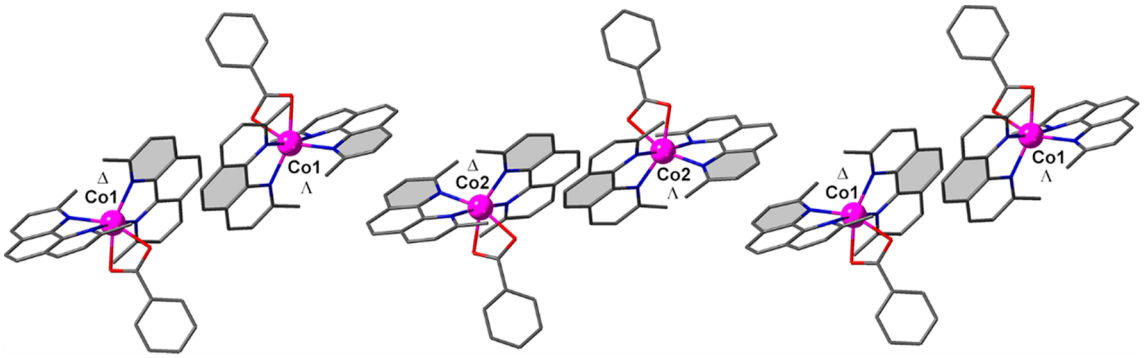

Figure 3. View of a fragment of the supramolecular chain in **1** extending through $\pi-\pi$ interactions (shaded aromatic rings). The perchlorate anions and crystallization solvent molecules are omitted for clarity.

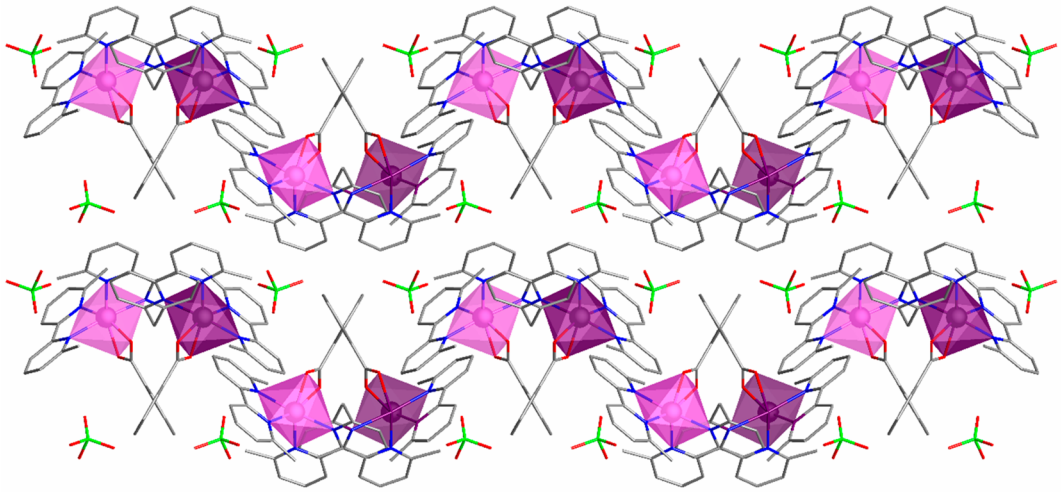

Figure 4. View of a fragment of the crystal packing in **2** extending across the crystallographic *c* axis.

for each one of the archetypal geometries, assigning a value which increases from zero (minimal distortion) as far as the degree of distortion of the ideal polyhedron increases. The values of the deviation from the minimal distortion pathway corresponding to the octahedron (OC-6) and trigonal prism (TPR-6) are 3.14 and 3.77 (OC-6) and 13.25 and 12.18 (TPR-6) for Co1 and Co2, respectively, in **1**, and 3.07 (OC-6) and 14.54 (TPR-6) for **2**. Consequently, the geometries of cobalt(II) ions in both complexes are similar, and they can be therefore viewed as distorted octahedra more than trigonal prisms. Among the two different metal centers in **1**, Co2 shows a more distorted geometry and, therefore, is further away from **2**. The loss of planarity in the benzoate ligand should have a role in this large distortion, but the greater asymmetry in the cobalt-to-oxygen bond lengths becomes probably the leading cause.

The crystal packings in **1** and **2** are quite different due to the presence of solvent molecules in the unit cell in the former compound. Hydrogen bonding involving the perchlorate anion and the water molecule [O1w···O5P^{i} = 2.867(6) Å] together with those between the water and methanol lattice molecules [O1w···O1M^{i} = 2.556(6) Å] occur in **1** [symmetry code: (i) = $1-x$, $1-y$, $1-z$]. Moreover, several $\pi-\pi$ type interactions (with centroid−centroid distances varying in the range 3.5−3.8 Å) are present in this compound concerning the phenanthroline rings between two equivalent [Co1···Co1^{i} = 8.978 Å and Co2···Co2^{ii} = 8.989 Å; symmetry code: (ii) = $-x$, $1-y$, $-z$] and also between crystallographically distinct metal atoms [Co1···Co2^{iii} = 9.325 Å; (iii) = x, $-1+y$, z] (see Table S1). As a result of all these $\pi-\pi$ interactions, a supramolecular chain is formed from a racemic mixture of (Δ, Λ)-Co1 and (Δ, Λ)-Co2 units (Figure 3). The shortest intermolecular cobalt−cobalt separation in **1** [7.511 Å for Co1···Co2^{iv}; (iv) = $1+x$, $-1+y$, z] deals with two crystallographically distinct complex cations, which only exhibit weak edge-to-face type interactions involving the pyridyl rings of dmphen and phenyl rings of the benzoate ligand (shortest centroid$_{OOCPh}$−carbon$_{dmphen}$ separation of 3.32 Å). The cobalt centers in **2** are well isolated from each other [shortest cobalt−cobalt separation of 7.925 Å for Co1···Co1^{v}; (v) = $2-x$, $-y$, $-z$], with the lack of significant intermolecular interactions being at the origin of this structural feature. Finally, it deserves to be noted a racemic mixture of isolated pairs of cobalt(II) motifs with (Δ, Λ) chirality occurs in **2**, as shown in Figure 4. In fact, both **1** and **2** crystallize in two centrosymmetric space groups.

FIRMS, HFEPR, Static (dc) Magnetic Properties, and Theoretical Calculations. Compounds **1** and **2** were investigated by a frequency domain magnetic resonance technique, far-infrared magnetic spectroscopy (FIRMS), which allowed us to directly probe the excitation from the $m_S = |\pm 1/2\rangle$ ground to the $m_S = |\pm 3/2\rangle$ first excited Kramers doublet, thus providing a direct measure of the *zfs* in both compounds. The resulting diagrams of turning points in the powder patterns are shown in Figure 5 as false-color (contour)

DOI: 10.1021/acs.inorgchem.9b01719
Inorg. Chem. 2019, 58, 15726−15740

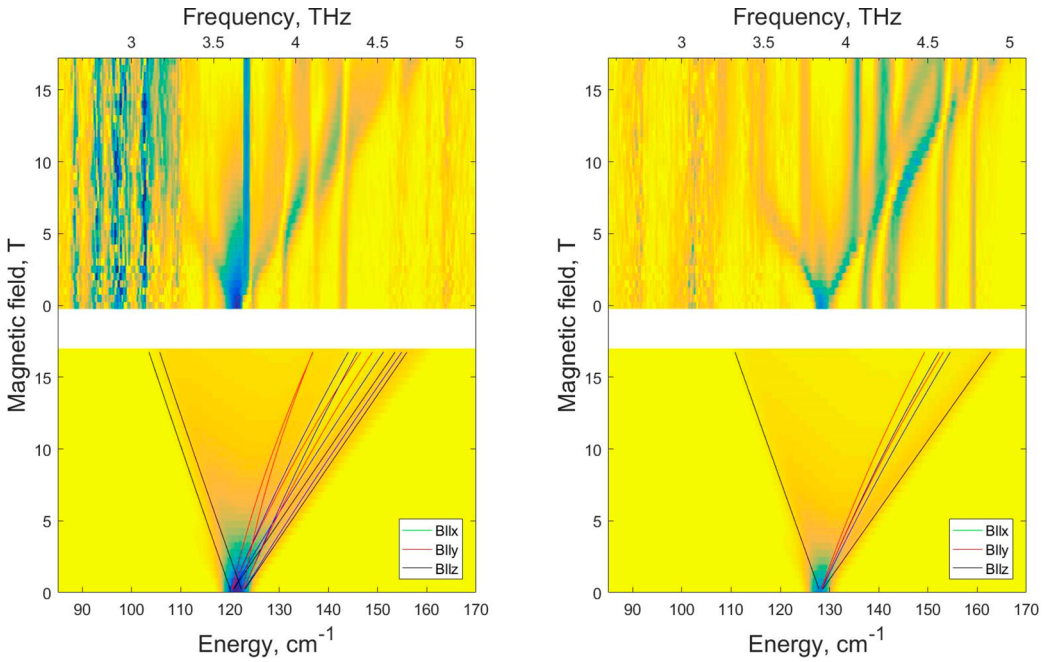

Figure 5. 2D maps of normalized transmittance spectra for **1** (left) and **2** (right) at 4.6 K. The top plots are experimental data. The tendency toward the blue color means the magnetic absorption increases, whereas the yellow color corresponds to the regions indifferent to the magnetic field. The patterns at low energies (<110 cm^{-1}) visible particularly in **1** are artifacts due to poor THz transparency of the sample in this spectral range. The vertical absorption features that do not change frequency with increasing field are appearing due to the coupling of the magnetic with nonmagnetic modes (phonons, intramolecular vibrations/rotations).[82] The lower plots are frequency-domain EPR simulations using the set of spin Hamiltonian parameters shown in Table 3. The lines superimposed on the simulated false-color maps show the position of the particular turning points on the 2D map.

Table 3. Best Values Found in 1 and 2 for the Parameters That Describe a Spin Hamiltonian Based on a *zfs* Approach with $S = 3/2$[a]

Technique	$g_\perp$[b]	$g_\parallel$[b]	D[c]	E/D[d]
1				
Magnetometry	2.55	2.28	+61.9	0.018
HFEPR	2.56(1)/2.58(1)	2.18(1)/2.21(1)	$D \gg 20$	0.147/0.187
FIRMS			+58.3[e]	
CASSCF/NEVPT2	2.545/2.525	2.029/2.038	+54.7/+51.5	0.219/0.226
2				
Magnetometry	2.57	2.01	+61.6	0.020
HFEPR	2.55(1)	2.22(1)	$D \gg 20$	0.052
FIRMS			+63.8[e]	
CASSCF/NEVPT2	2.574	2.016	+60.7	0.052

[a]These values were derived from a direct observation of the zero-field energy gaps by FIRMS, and through fits to the experimental data obtained by HFEPR and magnetometry, as well as by the theoretical study. Since two structurally different cobalt(II) complexes coexist in **1**, two sets of values (for Co1 and Co2) from CASSCF/NEVPT2 were obtained. [b]Values of the components of the Landé factor obtained from the fit of the magnetic susceptibility. [c]D is the axial magnetic anisotropy in cm^{-1}. [d]E/D unitless *zfs* rhombic factor magnetic anisotropy in cm^{-1}. [e]Assuming the *zfs* tensor is rhombic while the *g*-tensor is axial.

2D (field vs energy or frequency) maps of intensities. Most importantly, zero-field resonances of magnetic origin were detected by FIRMS at 121.3 and 128.2 cm^{-1} in **1** and **2**, respectively, corresponding to the desired inter-Kramers transition. Interpreting this result via a spin Hamiltonian as in eq 1, these values are equal to $2\sqrt{D^2 + 3E^2}$ (for a discussion of applicability of this Hamiltonian, see the magnetometry results below.)

$$\hat{H}_{zfs+Zeeman} = D\left[\hat{S}_z^2 - \frac{1}{3}S(S+1)\right] + E(\hat{S}_x^2 - \hat{S}_y^2) + \beta H[g_z\hat{S}_z + g_x\hat{S}_x + g_y\hat{S}_y] \quad (1)$$

where S is the spin ground state, D and E are the axial and transverse magnetic anisotropies, respectively, β is the Bohr magneton, and H is the applied magnetic field.

FIRMS was complemented by a field-domain technique, HFEPR, performed in the frequency range of 50−450 GHz, which resulted in powder patterns in **1** and **2** typical for an $S = 3/2$ spin state with very large ($|D| \gg 20$ cm^{-1}) and positive D (Figure S5), and consisting exclusively of turning points in the intra-Kramers transition within the $ms = |\pm 1/2\rangle$ manifold. The frequency dependencies of those turning points (Figure S6) allowed us to estimate the rhombic *zfs* parameters E and the *g*-values.[83] Since E is correlated with g_x and g_y, two limiting cases were considered: (a) the *zfs* tensor is rhombic, i.e. $E \neq 0$, but

DOI: 10.1021/acs.inorgchem.9b01719
Inorg. Chem. 2019, 58, 15726−15740

the g-tensor is axial, i.e. $g_x = g_y$, or (b) the *zfs* tensor is axial, i.e. $E = 0$, but the g-tensor is rhombic, i.e. $g_x \neq g_y$. The actual physical situation is somewhere between these two limits, but simulations showed that assuming a fully axial *zfs* tensor results in unphysical g_x or g_y values; therefore, taking into account the zero-field gap values obtained from FIRMS and the information from HFEPR, we ended up with the following estimates: 58.3 $cm^{-1} \leq D < 60.7$ cm^{-1}, $0 < E \leq 9.6$ cm^{-1} for **1**, and 63.8 $cm^{-1} \leq D < 64.1$ cm^{-1}, $0 < E \leq 3.3$ cm^{-1} for **2**. Since we believe case (a) above is more probable than (b), we placed the smaller values of D and the nonzero values of E in Table 3 together with axial g-tensor values.

Upon increasing the frequency, each of the turning points in the HFEPR spectrum of **1** is split (Figure S6) indicating the occurrence of two different $S = 3/2$ species with very similar but distinct *zfs* and g-tensors. These features agree with the presence of two crystallographically distinct cobalt(II) complexes in the crystal structure of **1** (Co1 and Co2). CASSCF/NEVPT2 calculations also show slight differences in the D, E/D ratio, and parallel and perpendicular components of the g-tensor between both centers. Figure S7 shows a spectrum at 208 GHz together with two simulations, each one using a different set of spin Hamiltonian parameters, which could correspond to the Co1 and Co2 centers.

The direct current magnetic properties (dc) of **1** and **2** as $\chi_M T$ versus T plots (χ_M being the dc magnetic susceptibility per Co^{II} ion) in the temperature range 2−300 K are depicted in Figure 6. At 300 K, the values of $\chi_M T$ are 2.97 (**1**) and 2.92 cm^3 mol^{-1} K (**2**). These values are higher than the spin-only value [$\chi_M T = (N\beta^2 g^2/3k_B)\, S\,(S+1) = 1.875$ cm^3 mol^{-1} K with $S = 3/2$ and $g = 2.0$], confirming the presence of an unquenched orbital contribution to the magnetic moment. Upon cooling, $\chi_M T$ for **1** and **2** exhibits a continuous decrease which becomes abrupt below 120 K, reaching values of 1.75 (**1**) and 1.72 (**2**) cm^3 mol^{-1} K at 2.0 K. The mononuclear complexes are well isolated from each other [the shortest cobalt−cobalt distances are larger than 8.978 (**1**) and 7.925 Å (**2**)]. This situation is also supported by the negligible intermolecular magnetic couplings (J) calculated from DFT calculations ($|J|$ less than *ca.* 0.002 cm^{-1}). These facts suggest that the magnetic properties of the two compounds obey to a strong first order spin−orbit coupling (SOC), as usually observed in octahedral cobalt(II) complexes.

Field-dependent magnetization studies were carried out at low temperatures for **1** and **2** (insets in Figure 6). The M values of 2.22 (**1**) and 2.18 $N\beta$ (**2**) at 50 kG are significantly below the saturation one for a high-spin d^7 Co^{II} ion ($M_{sat} = gSN\beta = 3\ N\beta$), suggesting thus the presence of a significant axial magnetic anisotropy of the octahedral high-spin Co^{II} ion in these compounds. Isothermal magnetization curves do not superimpose when a weak *zfs* or magnetic couplings are present. However, this is not the case when the value of the axial *zfs* ($|D|$) is substantial. In such a situation, the excited and ground Kramers doublet states are well separated in energy, and only the ground Kramers doublet is thermally populated. The reduced magnetization curves in **1** and **2** are close to superposition (Figure 6), a feature which is a clear signal of the presence of large $|D|$ values.

Taking advantage of the isomorphism between the T_1 and P terms,[84] the magnetic data of **1** and **2** were analyzed in the whole temperature range with the SOC Hamiltonian through eq 2 (black lines in Figure 6):

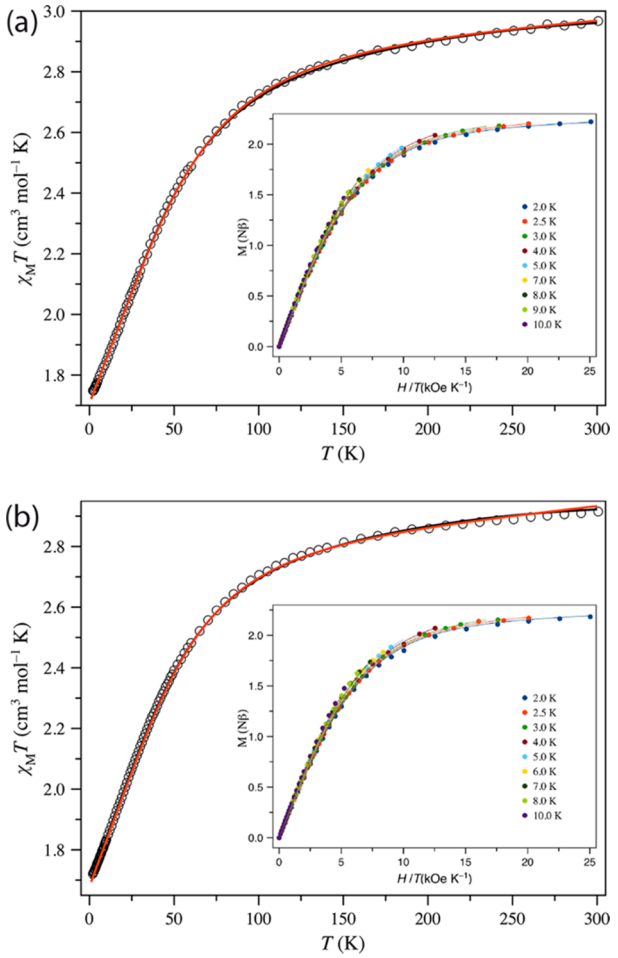

Figure 6. Temperature dependence of $\chi_M T$ under an applied dc field of 0.25 ($T < 30$ K) and 5.0 kG ($T \geq 20$ K) for **1** (a) and **2** (b). The inset shows the reduced magnetization curves at the indicated temperatures. The solid lines in both plots are the best-fit curves. Simulated temperature dependence of $\chi_M T$ through the 1st SOC and *zfs* models appear as black and red lines.

$$\hat{H} = -\alpha\lambda\hat{L}\hat{S} + \Delta[\hat{L}_z^{\,2} - L(L+1)/3] + \beta H[g_e\hat{S} - \alpha\hat{L}] \quad (2)$$

In this Hamiltonian, λ is the spin−orbit coupling parameter and α is an orbital reduction factor defined as $\alpha = A\kappa$. Whereas the κ parameter represents the reduction of the orbital momentum caused by the delocalization of the unpaired electrons, the A parameter makes up the contribution of the upper $^4T_{1g}(^4P)$ state into the $^4T_{1g}(^4F)$ ground state (A takes values of 1.5 and 1 in the weak and strong crystal-field limits, respectively). Additionally, under an axial distortion of the ideal O_h symmetry of the coordination sphere of the Co^{II} ion, the triplet orbital $^4T_{1g}$ splits into the singlet $^4A_2$ and doublet ^4E levels, separated by an energy gap described by the Δ parameter. The $^4A_2$ and ^4E levels split in turn by second-order spin−orbit coupling giving rise to two and four Kramers doublets, respectively. The best fit of the magnetic data with the VPMAG program[85] gave $\lambda = -130.8$ cm^{-1}, $\Delta = +591.8$ cm^{-1}, and $\alpha = 1.38$ with $F = 3.3 \times 10^{-6}$ for **1** and $\lambda = -133.0$ cm^{-1}, $\Delta = +606.1$ cm^{-1}, and $\alpha = 1.38$ with $F = 4.2 \times 10^{-6}$ for **2** (F is the agreement factor defined as $F = \sum[P_{exp} - P_{calcd}]^2/\sum[P_{exp}]^2$, with P being the measured physical property).

DOI: 10.1021/acs.inorgchem.9b01719
Inorg. Chem. 2019, 58, 15726−15740

Six Kramers doublets arise from the coupling between the spin (S = 3/2) and orbital (L = 1) momenta.[84,86−88] In a distorted octahedron, the two lowest doublets are usually the uniquely populated states below 50 K. Consequently, a phenomenological approach based on the zero-field splitting (*zfs*) in an S = 3/2 state considers only these two doublets [reflected by eq 3]. Therefore, the application of this approach at low temperatures is justified. Above 50 K, other Kramers doublets play a role in the magnetic behavior, and a temperature independent paramagnetism (TIP term) is introduced to account for the thermal depopulation of these remaining higher energy Kramers doublets. This strategy is usually efficient below 100 K and occasionally up to room temperature, and in the present case, it allowed us to analyze the magnetic data of **1** and **2** in the 2.0−300 K temperature range. The magnetic properties of **1** and **2** were thus also interpreted through the following spin Hamiltonian, differing from eq 1 only by an implicit assumption of an axial g-tensor [eq 3]:

$$\hat{H}_{zfs+Zeeman} = D\left[\hat{S}_z^2 - \frac{1}{3}S(S+1)\right] + E(\hat{S}_x^2 - \hat{S}_y^2) + \beta H[g_{\parallel}\hat{S}_z + g_{\perp}(\hat{S}_x + \hat{S}_y)] \quad (3)$$

In this model, the energy gap between the ±1/2 and ±3/2 doublets is 2|D| when E = 0. By convention, when the M_S = ±1/2 Kramers doublet is lower on the energy scale, D is positive. When the M_S = ±3/2 doublet is lower, D is negative. The nonsuperposition of the magnetization (M) versus H/T plots for **1** and **2** on a single master curve supports the presence of significant magnetic anisotropy in them [see insets of Figure 6]. However, the curves are not very different, evidencing that the D values are very large and the changes in the thermal depopulation of the two Kramers doublets below 10 K are almost irrelevant. Occasionally, this situation prevents an accurate evaluation of the parameters that determine the *zfs* tensor. Nevertheless, the magnetization data at different applied dc fields and temperatures and the variable-temperature magnetic susceptibility data of **1** and **2** could be analyzed simultaneously by using the *VPMAG* package and the above Hamiltonian. The best-fit values of the susceptibility data through the *VPMAG* program are D = +61.9 cm^{-1}, E/D = 0.018, $g_{\perp}$ = 2.55, $g_{\parallel}$ = 2.28, and TIP × 10^6 = 400 cm^3 mol^{-1} with F = 3.1 × 10^{-5} for **1** and D = +61.6 cm^{-1}, E/D = 0.020, $g_{\perp}$ = 2.57, $g_{\parallel}$ = 2.01, and TIP × 10^6 = 650 cm^3 mol^{-1} with F = 2.5 × 10^{-5} for **2**. It deserves to be noted that whereas a good agreement between the experimental and calculated curves is obtained for both compounds with positive values of D (Figure 6), no reasonable fits were obtained for negative D values. The $g_{\parallel}$ values of **1** and **2** are found different, and E/D is too small in **1**, which is not confirmed in HFEPR spectra and is most likely an artifact arising during the fits. Among its possible causes are the high correlation between the parameters $g_{\perp}$, $g_{\parallel}$, and E/D shown in the simulation of the magnetic curves ($\chi_M T$ vs T and M vs H/T) and the high D value that leads to the collapse of the reduced magnetization curves and, therefore, to a difficulty in evaluating the E/D ratio and the components of the g-tensor. Magnetometry, although useful, often shows certain limitations, compared to other experimental and theoretical techniques (see below). Because the ground state is a ±1/2 Kramers doublet, the system can be considered an effective S = 1/2. The energy gap between the lowest Kramers doublets connects both models, first order SOC and *zfs*, which provide close values for each compound [124.6 (SOC) and 124.1 cm^{-1} (*zfs*), and 125.1 (SOC) and 123.6 cm^{-1} (*zfs*) for **1** and **2**, respectively], validating the use of both approaches. The resemblance found in the coordination sphere of the cobalt(II) ions in **1** and **2** is at the origin of the similar but not identical energy gaps obtained for them.

The numerical analysis was done based on the D-values delivered by FIRMS, magnetometry, and CASSCF/NEVPT2 calculations, using the multifrequency HFEPR data sets (Figure S6). This analysis established a positive sign of D in agreement with the magnetometry and CASSCF/NEVPT2 calculations (see below and Table 3). It also provided moderate values of the rhombicity factor |E/D| [0.167 (**1**) and 0.052 (**2**)]. In particular, the comparison between simulations with positive and negative D values and the experimental spectra recorded at 4.5 K and at 52 GHz frequency rules out any doubt about its positive sign, where the presence of signals for **1** at applied magnetic fields of 1.0 and 1.8 T and their absence around 3 T becomes determinant (Figure S5(a)). The large D value is also correlated with the perpendicular and parallel components of the g-tensor [$g_{\perp}$ = 2.57, $g_{\parallel}$ = 2.195; and $g_{\perp}$ = 2.55, $g_{\parallel}$ = 2.28 for **1** and **2**, respectively] (Table 3). In agreement with a positive D value, the perpendicular components of the g-tensor are larger than the parallel one.[25] This picture is similar to that provided by magnetometry, but there are some minor discrepancies, in particular in the E/D ratio, with its evaluation with the latter technique being a difficult task because of the quasi-collapse of the M vs H/T curves. The larger E/D ratio observed in **1** compared to **2** may be a consequence of the fact that the coordination sphere of the metal center in **1** is farther from the ideal octahedron than in **2**, as shown by the shape measurements and mainly validated by the greater asymmetry in the equatorial cobalt-to-oxygen bond lengths (see above).

Theoretical CASSCCF/NEVPT2 calculations were performed to confirm the sign and magnitude of the D parameter as well as the E/D quotients of both compounds (see Table 3), measured by FIRMS and estimated by HFEPR spectroscopy and magnetometry. These calculations unambiguously support a positive sign of D in the two compounds, with their values being very large [D = +54.7 (Co1), +51.5 cm^{-1} (Co2) in **1** and +60.7 cm^{-1} in **2**]. Even though there are two structurally different cobalt(II) complexes in **1**, both of them keep the positive sign and similar values of D. The larger values of the E/D ratio of the two complexes in **1** [0.219 (Co1) and 0.226 (Co2)] compared to **2** (0.052) agree with the HFEPR results and follow the greater asymmetry of the equatorial Co−O bond lengths (d_{CoO}) evaluated from the parameter δ, defined as 200 × |$d_{CoO1} - d_{CoO2}$|/($d_{CoO1} + d_{CoO2}$), [2.39 (Co1) and 4.86 (Co2) in **1** and 0.60 in **2**]. The fact that Co1 and Co2 in **1** show similar values of the parameters describing the *zfs* tensor supports the approach to analyze the experimental data considering only one metal center. This large *zfs* is translated to the calculated g-tensor, with the perpendicular components being substantially greater than the parallel ones [$g_{\perp}$ = 2.545 (Co1), 2.525 (Co2) in **1** and 2.574 in **2**; and $g_{\parallel}$ = 2.029 (Co1) and 2.038 (Co2) in **1**, and 2.016 in **2**]. This feature, already observed with the experimental studies, is a consequence of the positive D value. In brief, a good agreement is observed in both compounds with the results from FIRMS, HFEPR, and magnetometry. The contributions of other excited states are almost negligible because they are far above the ground state on the energy scale. The more significant spin−orbit

DOI: 10.1021/acs.inorgchem.9b01719
Inorg. Chem. 2019, 58, 15726−15740

contributions mainly originate from the quartet states (D_Q)—more specifically from the two first excited states (Q_1 and Q_2), rather than from the doublet ones (D_D), with the relative energy of each excited state (Δ_i) governing the magnitude of its input [Tables S2 (**1**) and S3 (**2**)]. As a consequence of some geometrical distortions, the $^4T_{1g}$ ground state splits into the ground and the Q_1 and Q_2 excited states. Then, these excited states are very close to the ground one [979 and 1686 cm^{-1} (Co1), 1026 and 1791 cm^{-1} (Co2) in **1**, and 1018 and 1301 cm^{-1} in **2**] and their contributions to D are significantly larger. On the other hand, the greater energy gap arising between two low-lying excited states (Q_1 and Q_2) is the cause of a more significant *zfs* rhombicity in **1** (Table S2).

Dynamic Magnetic Behavior. In order to explore the SIM behavior of **1** and **2**, frequency dependent alternating current (ac) magnetic susceptibility measurements below 10 K down to 2.0 K were investigated under several applied static fields in the range 0−2.5 kG [Figures 7 and S8 (**1**), and 8 and S9 (**2**)]. No out-of-phase signal (χ''_M) is observed in the absence of an external magnetic field for both compounds. However, the application of an external static field results in the emergence of strong frequency-dependent χ_M' and χ_M'' signals. This feature, usually observed in octahedral cobalt(II) complexes, is a clear sign of the occurrence of fast tunneling of the magnetization (QTM) that is removed under nonzero applied dc fields.[16] Whereas **1** shows only a single signal below 7 K at all dc magnetic fields, a shoulder (on both χ'_M and χ''_M), whose intensity increases with the frequency for a given field, is observed in **2** together with the single signal (Figures 8 and S9). These phenomena are typical of SIM behavior.

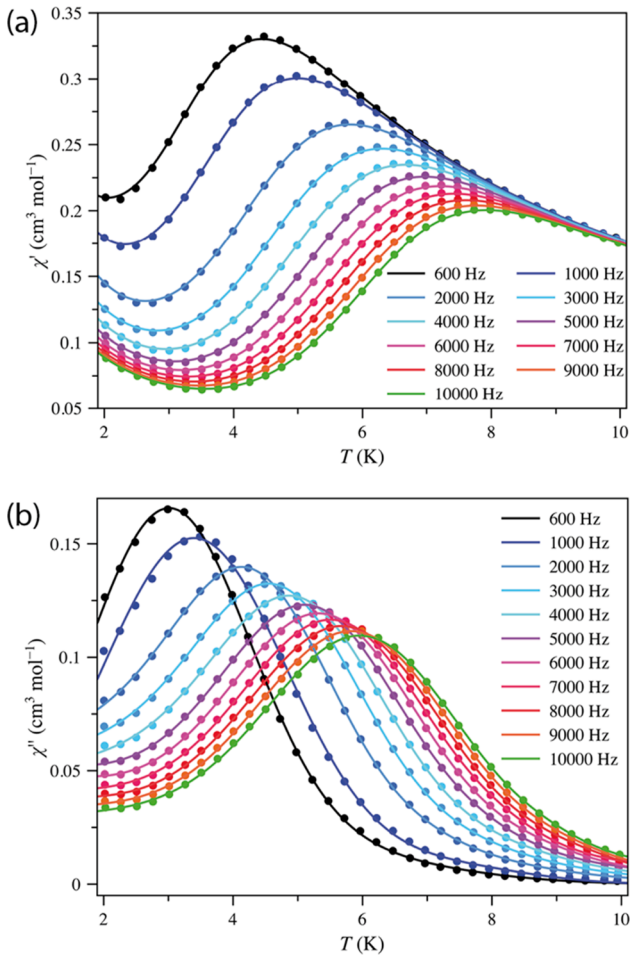

Figure 7. Temperature dependence of χ'_M (a) and χ''_M (b) of **1** in an applied dc field of 1.0 kG and under ±5.0 G oscillating field at frequencies in the range of 0.6 (black) to 10.0 (green) kHz. The filled circles and solid lines are experimental data and simulated curves, respectively.

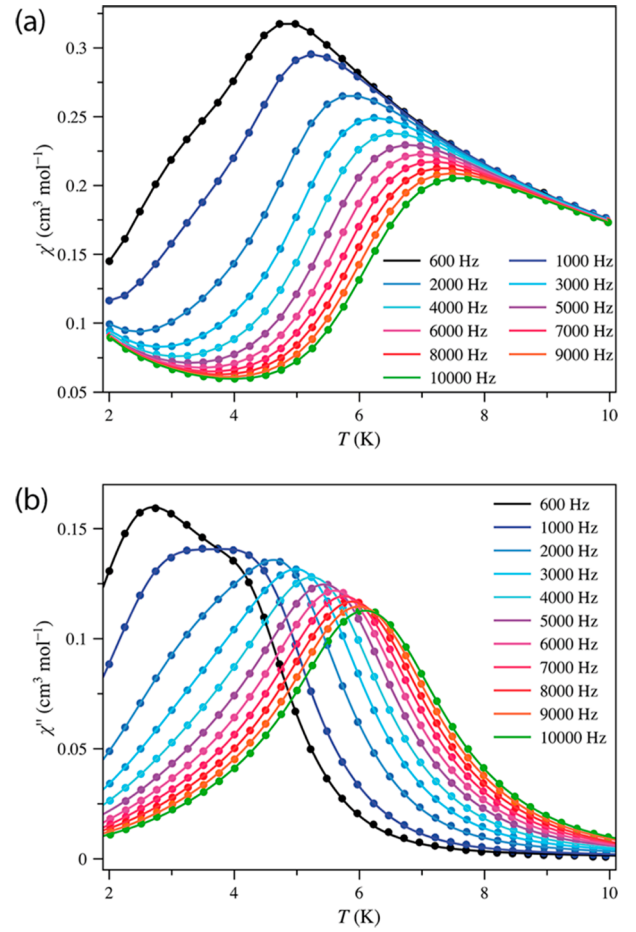

Figure 8. Temperature dependence of χ'_M (a) and χ''_M (b) of **2** in an applied dc field of 1.0 kG and under ±5.0 G oscillating field at frequencies in the range of 0.6 (black) to 10.0 (green) kHz. The filled circles and solid lines are experimental data and simulated curves, respectively.

The Cole−Cole plots in the 5.0−6.5 K temperature range under different applied *dc* fields for both compounds show quasi-perfect semicircles whose fits were done by using the Debye model [Figures 9 (**1** and **2**, H_{dc} = 1.0 kG) and S10 (**1** and **2**, H_{dc} = 0.5 and 2.5 kG)].[89] The values of α cover the ranges 0.048 (6.5 K)−0.192 (5.0 K) and 0.021 (6.5 K)−0.142 (5.0 K) for **1** and **2**, respectively (see Table S4). Having in mind that α values equal to 1 and 0 correspond to infinitely wide distribution and one unique value of relaxation times, respectively, **1** and **2** are closer to the second case. As far as the temperature is decreased, additional relaxation mechanisms become inoperative, and this is evidenced in the ac measurements, supporting the greater α values at low temperatures. However, in the present case, the larger α values in **1** compared to **2** could be related to the occurrence of two crystallographically independent cobalt(II) complexes in **1**.

DOI: 10.1021/acs.inorgchem.9b01719
Inorg. Chem. 2019, 58, 15726−15740

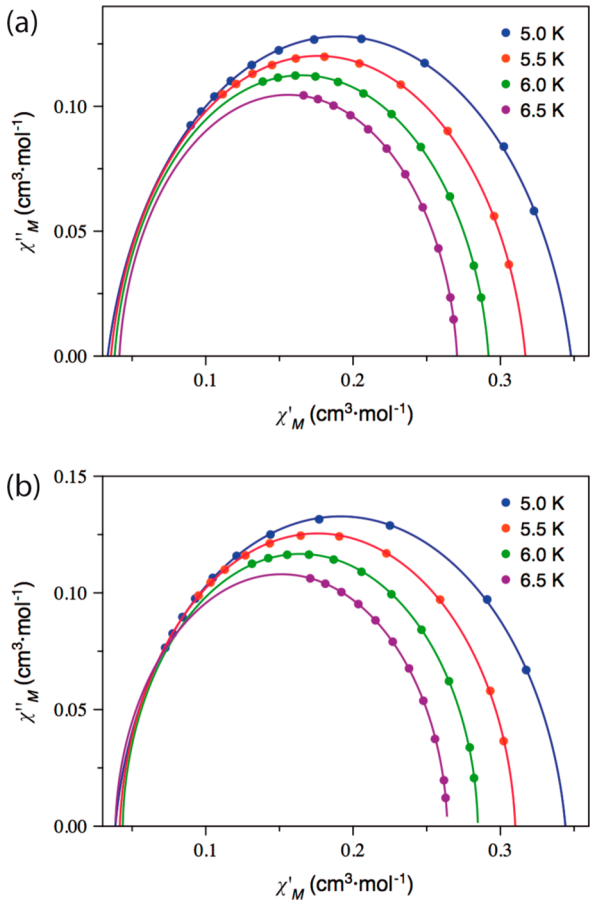

Figure 9. Cole−Cole plots at 5.0 K (blue dots), 5.5 K (red dots), 6.0 K (green dots), and 6.5 K (purple dots) under an applied dc field of 1.0 kG for **1** (a) and **2** (b). Solid lines represent the best fit (see text).

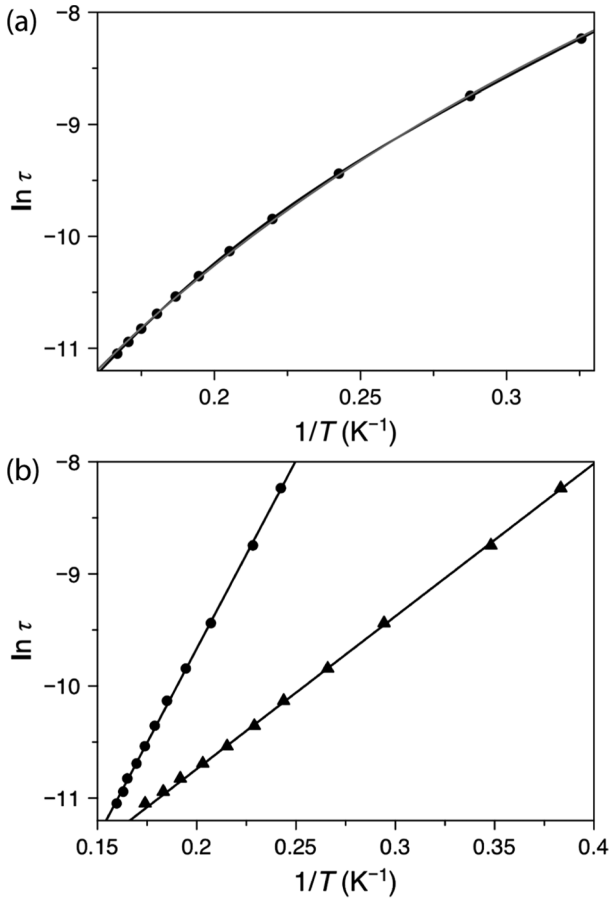

Figure 10. Arrhenius plots under an applied dc field of 1.0 kG for **1** (a) and **2** (b). Solid lines represent the best fit (see text) through the models described in eqs 4 [Orbach + Orbach, in black] and 6 [Raman, in gray]. Error bars do not appear because they are smaller than the dots used to visualize the experimental data (standard deviation in $1/T$ less than 0.002).

The relaxation times of **1** and **2** calculated from the maxima of χ''_M at a given frequency ($\tau = 1/2\pi\nu$) were used to build the corresponding Arrhenius plots [Figures 10 (**1** and **2**, H_{dc} = 1.0 kG) and S11 (**1** and **2**, H_{dc} = 0.5 and 2.5 kG)]. The deviation of the linearity observed in **1** is often attributed to the presence of several competing relaxation mechanisms (Orbach, direct, Raman and quantum tunneling).[90] Even though all these mechanisms can play a role in the slow relaxation of the magnetization, the use of all of them to analyze the experimental Arrhenius plots is unrealistic. Therefore, the quantum-tunneling is the first mechanism to be excluded because no sign of its effects on the Arrhenius plots is usually detected above 2.0 K. On the other hand, in our previous works on octahedral cobalt(II) complexes, it was observed that two or more competing relaxation processes work better when the Raman mechanism ($\tau^{-1} = CT^n$) is ruled out.[24,25,43] In such cases, the exponential n factor significantly deviates from the expected values for a Raman process (n values between 6 and 8) either for all or some of the applied dc fields. Also, the C factor does not usually follow the expected magnetic field dependence. Anyway, this mechanism cannot be systematically discarded. The use of a combination of Orbach and direct mechanisms [eq 4] gave good results in the past, but they were poorer than those obtained through two competing Orbach processes [eq 5].[25] A discussion on the application of these three mechanisms follows here, with the more relevant results being listed in Tables S4 and S5.

$$\tau^{-1} = \tau_{01}^{-1} e^{-E_{a1}/k_B T} + AT \quad (4)$$

$$\tau^{-1} = \tau_{01}^{-1} e^{-E_{a1}/k_B T} + \tau_{02}^{-1} e^{-E_{a2}/k_B T} \quad (5)$$

$$\tau^{-1} = CT^n + AT \quad (6)$$

$$\tau^{-1} = CT^n \quad (7)$$

$$\tau^{-1} = \tau_{01}^{-1} e^{-E_{a1}/k_B T} + CT^n \quad (8)$$

Although the combination of Orbach plus direct mechanisms [eq 4] correctly simulates the Arrhenius plots of **1**, there is no clear dependence on the applied magnetic field of the values of the parameters that define these processes. This feature together with the emergence of the negative values of the A coefficient when Raman and direct processes are competing [eq 6] lead to rule out any option in which the direct mechanism could be present. Despite some nonconvincing results in the past using only a Raman mechanism [eq 7], the analysis of the Arrhenius plots for **1** seems reasonable, and there are definite trends between their preexponential and exponential coefficients and the external dc magnetic field. Nevertheless, the standard deviations for these values are significant and the exponential n factor, even if it remains almost constant, takes values about 4, which is out of the normal range (n = 6−8). This fact is reproduced, and even gets

DOI: 10.1021/acs.inorgchem.9b01719
Inorg. Chem. 2019, 58, 15726−15740

worse at lowest applied dc field, when Orbach and Raman are simultaneously considered (eq 8 and Table S5). Like in the past, the association of two Orbach processes provides the best simulations (Figures 10 and S11), displaying explicit dependences of the exponential (τ_0) and preexponential (E_a) coefficients on the applied dc magnetic field. Table S4 shows how the values of τ_0 increase with the intensifying applied dc field, whereas those of the activation energy (E_a) slightly decrease for the first relaxation process. Dealing with the second relaxation process, the values of τ_0 follow the opposite trend to the first one, and those of the E_a remain almost constant. Although one of the processes is governing the SIM behavior in the almost complete range of the Arrhenius plot for H_{dc} = 500 G, we were able to report results for both processes. This situation points out that it is possible to give priority to a particular mechanism by modifying H_{dc}.

The main issue in this context is to know the physical meaning of the energy barrier (E_a) being well established that the positive sign of the axial component (D) of the *zfs* tensor prevents the emergence of any energy barrier. Even though some models were envisaged in the past to account for this circumstance,[16,26,91] an approach based on the vibrational modes of the isolated molecule or the solid network through a spin-phonon coupling recently makes one's way.[82,92−94] In our opinion, these energy barriers are bound to the lowest vibrational modes of the metal complex. In this way, when these vibrational modes are thermally populated, the relaxation of the magnetization becomes faster, causing the removal of the blocking of the magnetization. In this sense, the three lowest vibrational modes calculated for the optimized geometry of **1** (15.0, 19.0, and 28.5 cm^{-1}) are close to the experimental E_a values (see Table S4 and 4). According to this hypothesis, the greater value of E_a could be linked to a second vibrational mode or a more energetic level of the same vibrational mode. To be confident of the quality of the calculated vibrational frequencies to compare them with the energy barriers, we have set side by side the more significant signals from the experimental IR spectra of **1** and **2** with their equivalent theoretical values (see Table S6). However, in the present discussion, the interest is focused on the lower-energy frequencies. Fortunately, some nonmagnetic transitions occur in the FIRMS spectra, and they can be used for this test (see Table S6). In all cases, the theoretical values match well with the experimental data at high- and low-energies, and the deviation between them is ever smaller than three percent. Therefore, a comparison between the vibrational frequencies and energy barriers is possible, supporting our last conclusion about a viable relaxation of the magnetization governed by some vibrational modes or a spin-phonon coupling.

In contrast to what occurs in **1** where a single out-of-phase signal is observed, a peak and a shoulder are present for **2** at any applied dc field. This fact indicates that at least two competing relaxation processes are operative in this compound. To properly analyze them, we have carried out a deconvolution of the χ''_M vs T curves, and the corresponding sets of signals were treated in an independent way. Figures 10 (H_{dc} = 1.0 kG) and S11 (H_{dc} = 0.5 and 2.5 kG) show the Arrhenius plots where the two coexistent mechanisms lead to a linear dependence of $\ln(\tau)$ against $1/T$ on both plots. A priori, the extracted data from this deconvolution should be only reliable for the cases where the shoulder in the χ''_M vs T curves is clearly visible. However, all Arrhenius plots are linear in the whole range of the studied frequencies of the oscillating magnetic field. This linear dependence demonstrates that neither Raman nor direct relaxation processes can be involved and only an Orbach mechanism has to be considered as a real candidate. The results obtained in the context of the model based on two Orbach processes for **2** (Table S4) are similar to those found for **1**. Notably, the values of E_a are of the same order of magnitude in both compounds, with this being a signature of the equivalence between the relaxation mechanisms in **1** and **2**. Therefore, because of the same coordination surrounding and similar geometries for the coordination sphere in the X-ray structures of **1** and **2**, also supported by magnetometry, HFEPR, and theoretical studies, both molecules relax in the same way. Thus, the two observed independent relaxations in **2** are those previously found together in **1**. This last situation is the usual one in mononuclear octahedral cobalt(II) complexes and even in compounds with other transition metal ions where the authors have often assumed one Raman process as the fundamental mechanism for the slow relaxation of the magnetization. In the light of our results on **2**, this assumption should be no longer valid. On the other hand, a previous interpretation of the slow relaxation magnetization in easy-plane cobalt(II) mononuclear complexes through a classical in-plane barrier arising from a rhombicity in the spin Hamiltonian should be discarded because both compounds show similar dynamic behavior, but they exhibit very different values of the E/D ratio.

To verify the specific response observed for **1** and **2**, particularly for **2**, we have also studied their dynamic behavior from the χ''_M vs ν isothermal curves (Figure S12). These graphs are similar for both compounds, and now no binary signals were observed for **2**. However, the analysis of the Arrhenius plots through a model based on two competing Orbach processes provides similar energy barriers to those previously obtained (Figure S13 and Table S7). Therefore, the conclusions previously set out were confirmed. Both the thermal and frequency dependence of χ''_M have been useful for the study of **1** and **2**; however, in this case, the former approach provided more information distinguishing the two relaxation processes in **2**.

Once more, the vibrational calculation for **2** provides energies equal to 11.0, 20.2, and 21.1 cm^{-1} for the low-lying vibrational modes, values which are similar to those of E_a (Table 4). Additionally, these vibrational energies are slightly smaller than those in **1**, as also observed for E_a. Even though this study cannot be conclusive about the origin of the slow relaxation of the magnetization, it does for the Orbach nature of the relaxation mechanism, and moreover, it provides strong support to the main role played by the lowest vibrational modes on this physical phenomenon.

Table 4. Summary of the Values (in cm^{-1}) of the Energy Barriers (E_a) and Low-Energy Vibrational Modes (ν_i) Found for 1 and 2

Compound	E_{a1}	E_{a2}	ν_1	ν_2	ν_3
1	6.9−9.8	26.5−27.3	15.0	19.0	28.5
2	8.5−10.1	22.0−23.5	11.0	20.2	21.1

CONCLUSIONS

The two cobalt(II) complexes **1** and **2** exhibit a strongly distorted CoN_4O_2 octahedral environment, with the main source for the observed distortion being due to the reduced

DOI: 10.1021/acs.inorgchem.9b01719
Inorg. Chem. 2019, 58, 15726−15740

bite of the chelating carboxylate group. This group together with the bulky dmphen (**1**) and dmbipy (**2**) molecules were used as ligands toward the cobalt(II) ion aiming to induce a high distortion of its coordination sphere. The two crystallographically independent cobalt(II) ions in **1** show the same donor set and very close bond lengths and angles. The cryomagnetic properties of **1** and **2** were investigated by low-temperature FIRMS and HFEPR spectroscopies, static and dynamic magnetic susceptibility measurements, and *ab initio* calculations. Both complexes exhibit an easy-plane type anisotropy, and an out-of-phase magnetic susceptibility was observed for them under applied dc fields. The detailed analysis of the relaxation of the magnetization revealed the presence of either two Orbach or one Orbach plus a direct mechanisms for **1** whereas two independent relaxation processes occur in **2**, with each one obeying linear dependences of ln τ vs $1/T$. This feature demonstrates that neither Raman nor direct relaxation processes can be involved in both compounds and most likely in other cobalt(II) SIMs. The values of E_a are of the same order of magnitude for both compounds demonstrating the equivalence between the relaxation mechanisms in **1** and **2**. Theoretical calculations confirm the easy-plane anisotropy for **1** and **2** and reveal the stronger rhombic distortion of the magnetic anisotropy in **1** with respect to **2**. These results combined with those of FIRMS and HFEPR allowed us to assign an E/D value to each of the independent cobalt(II) sites which coexist in **1**. Finally, theoretical energies for the low-lying vibrational modes point out a spin-phonon coupling as the underlying factor governing the relaxation of the magnetization, where activation and vibrational energies are closely related.

■ ASSOCIATED CONTENT

Supporting Information

The Supporting Information is available free of charge on the ACS Publications website at DOI: 10.1021/acs.inorgchem.9b01719.

XRPD, infrared spectra, crystallographic drawings and tables, HFEPR spectra, magnetic data and *ab initio* calculations (PDF)

Accession Codes

CCDC 1914219−1914220 contain the supplementary crystallographic data for this paper. These data can be obtained free of charge via www.ccdc.cam.ac.uk/data_request/cif, or by emailing data_request@ccdc.cam.ac.uk, or by contacting The Cambridge Crystallographic Data Centre, 12 Union Road, Cambridge CB2 1EZ, UK; fax: +44 1223 336033.

■ AUTHOR INFORMATION

Corresponding Authors

*E-mail: krzystek@magnet.fsu.edu.
*E-mail: giovanni.demunno@unical.it.
*E-mail: joan.cano@uv.es.

ORCID

Marta Viciano-Chumillas: 0000-0001-7997-5908
Francisco Lloret: 0000-0003-2959-0879
Miguel Julve: 0000-0001-9006-8268
J. Krzystek: 0000-0001-6088-1936
Mykhaylo Ozerov: 0000-0002-5470-1158
Donatella Armentano: 0000-0002-8502-8074
Giovanni De Munno: 0000-0003-0071-0734
Joan Cano: 0000-0002-7382-7135

Notes

The authors declare no competing financial interest.

■ ACKNOWLEDGMENTS

This work was financially supported by Ministerio Español de Ciencia e Innovación (Projects CTQ2016-75068P and CTQ2016-75671P), Unidad de Excelencia María de Maetzu (MDM-2015-0538), and the Ministero dell'Istruzione, dell'Università e della Ricerca (Italy). D.A. thanks the "Fondo per il finanziamento delle attività base di ricerca". J.V. and M.V.-C. acknowledge the Spanish Ministry for research fellowships. FIRMS and HFEPR studies were supported by the NHMFL, which is funded by the NSF through a Cooperative Agreement DMR 1644779 and the State of Florida. We thank A. Ozarowski for his EPR simulation and fit software SPIN.

■ REFERENCES

(1) Gatteschi, D.; Sessoli, R.; Villain, J. *Molecular Nanomagnets*; Oxford University Press, 2006. .

(2) Aromí, G.; Brechin, E. K. Synthesis of 3d Metallic Single-Molecule Magnets. In *Single-Molecule Magnets and Related Phenomena*; Springer-Verlag: Berlin/Heidelberg, pp 1−67. .

(3) Christou, G. Single-Molecule Magnets: A Molecular Approach to Nanoscale Magnetic Materials. *Polyhedron* **2005**, *24* (16−17), 2065−2075.

(4) Ruiz, E.; Cirera, J.; Cano, J.; Alvarez, S.; Loose, C.; Kortus, J. Can Large Magnetic Anisotropy and High Spin Really Coexist? *Chem. Commun.* **2008**, *2* (1), 52−54.

(5) Neese, F.; Pantazis, D. A. What Is Not Required to Make a Single Molecule Magnet. *Faraday Discuss.* **2011**, *148*, 229−238.

(6) Rinehart, J. D.; Long, J. R. Exploiting Single-Ion Anisotropy in the Design of f-Element Single-Molecule Magnets. *Chem. Sci.* **2011**, *2* (11), 2078.

(7) Woodruff, D. N.; Winpenny, R. E. P.; Layfield, R. A. Lanthanide Single-Molecule Magnets. *Chem. Rev.* **2013**, *113* (7), 5110−5148.

(8) Tang, J.; Zhang, P. *Lanthanide Single Molecule Magnets*; Springer Berlin Heidelberg: Berlin, Heidelberg, 2015. .

(9) Ishikawa, N.; Sugita, M.; Ishikawa, T.; Koshihara, S.; Kaizu, Y. Lanthanide Double-Decker Complexes Functioning as Magnets at the Single-Molecular Level. *J. Am. Chem. Soc.* **2003**, *125* (29), 8694−8695.

(10) Rinehart, J. D.; Long, J. R. Slow Magnetic Relaxation in a Trigonal Prismatic Uranium(III) Complex. *J. Am. Chem. Soc.* **2009**, *131* (35), 12558−12559.

(11) Freedman, D. E.; Harman, W. H.; Harris, T. D.; Long, G. J.; Chang, C. J.; Long, J. R. Slow Magnetic Relaxation in a High-Spin Iron(II) Complex. *J. Am. Chem. Soc.* **2010**, *132* (4), 1224−1225.

(12) Harman, W. H.; Harris, T. D.; Freedman, D. E.; Fong, H.; Chang, A.; Rinehart, J. D.; Ozarowski, A.; Sougrati, M. T.; Grandjean, F.; Long, G. J.; et al. Slow Magnetic Relaxation in a Family of Trigonal Pyramidal Iron(II) Pyrrolide Complexes. *J. Am. Chem. Soc.* **2010**, *132* (51), 18115−18126.

(13) Zadrozny, J. M.; Long, J. R. Slow Magnetic Relaxation at Zero Field in the Tetrahedral Complex [Co(SPh)4]2−. *J. Am. Chem. Soc.* **2011**, *133* (51), 20732−20734.

(14) Jurca, T.; Farghal, A.; Lin, P. H.; Korobkov, I.; Murugesu, M.; Richeson, D. S. Single-Molecule Magnet Behavior with a Single Metal Center Enhanced through Peripheral Ligand Modifications. *J. Am. Chem. Soc.* **2011**, *133* (40), 15814−15817.

(15) Vallejo, J.; Pascual-Álvarez, A.; Cano, J.; Castro, I.; Julve, M.; Lloret, F.; Krzystek, J.; De Munno, G.; Armentano, D.; Wernsdorfer, W.; et al. Field-Induced Hysteresis and Quantum Tunneling of the Magnetization in a Mononuclear Manganese(III) Complex. *Angew. Chem., Int. Ed.* **2013**, *52* (52), 14075−14079.

(16) Vallejo, J.; Castro, I.; Ruiz-García, R.; Cano, J.; Julve, M.; Lloret, F.; De Munno, G.; Wernsdorfer, W.; Pardo, E. Field-Induced

DOI: 10.1021/acs.inorgchem.9b01719
Inorg. Chem. 2019, 58, 15726−15740

Slow Magnetic Relaxation in a Six-Coordinate Mononuclear Cobalt-(II) Complex with a Positive Anisotropy. *J. Am. Chem. Soc.* **2012**, *134* (38), 15704−15707.
(17) Poulten, R. C.; Page, M. J.; Algarra, A. G.; Le Roy, J. J.; López, I.; Carter, E.; Llobet, A.; Macgregor, S. A.; Mahon, M. F.; Murphy, D. M.; et al. Synthesis, Electronic Structure, and Magnetism of [Ni(6-Mes)2]+: A Two-Coordinate Nickel(I) Complex Stabilized by Bulky N-Heterocyclic Carbenes. *J. Am. Chem. Soc.* **2013**, *135* (37), 13640−13643.
(18) Craig, G. A.; Murrie, M. 3d Single-Ion Magnets. *Chem. Soc. Rev.* **2015**, *44* (8), 2135−2147.
(19) Colacio, E.; Ruiz, J.; Ruiz, E.; Cremades, E.; Krzystek, J.; Carretta, S.; Cano, J.; Guidi, T.; Wernsdorfer, W.; Brechin, E. K. Slow Magnetic Relaxation in a CoII-YIII Single-Ion Magnet with Positive Axial Zero-Field Splitting. *Angew. Chem., Int. Ed.* **2013**, *52* (35), 9130−9134.
(20) Zhu, Y.-Y.; Cui, C.; Zhang, Y.-Q.; Jia, J.-H.; Guo, X.; Gao, C.; Qian, K.; Jiang, S.-D.; Wang, B.-W.; Wang, Z.-M.; et al. Zero-Field Slow Magnetic Relaxation from Single Co(II) Ion: A Transition Metal Single-Molecule Magnet with High Anisotropy Barrier. *Chem. Sci.* **2013**, *4* (4), 1802−1806.
(21) Gomez-Coca, S.; Cremades, E.; Aliaga-Alcalde, N.; Ruiz, E. Mononuclear Single-Molecule Magnets: Tailoring the Magnetic Anisotropy of First-Row Transition-Metal Complexes. *J. Am. Chem. Soc.* **2013**, *135* (18), 7010−7018.
(22) Herchel, R.; Váhovská, L.; Potočňák, I.; Trávníček, Z. Slow Magnetic Relaxation in Octahedral Cobalt(II) Field-Induced Single-Ion Magnet with Positive Axial and Large Rhombic Anisotropy. *Inorg. Chem.* **2014**, *53* (12), 5896−5898.
(23) Zhu, Y.-Y.; Zhu, M.-S.; Yin, T.-T.; Meng, Y.-S.; Wu, Z.-Q.; Zhang, Y.-Q.; Gao, S. Cobalt(II) Coordination Polymer Exhibiting Single-Ion-Magnet-Type Field-Induced Slow Relaxation Behavior. *Inorg. Chem.* **2015**, *54* (8), 3716−3718.
(24) Vallejo, J.; Fortea-Pérez, F. R.; Pardo, E.; Benmansour, S.; Castro, I.; Krzystek, J.; Armentano, D.; Cano, J. Guest-Dependent Single-Ion Magnet Behaviour in a Cobalt(II) Metal−Organic Framework. *Chem. Sci.* **2016**, *7* (3), 2286−2293.
(25) Świtlicka, A.; Palion-Gazda, J.; Machura, B.; Cano, J.; Lloret, F.; Julve, M. Field-Induced Slow Magnetic Relaxation in Pseudooctahedral Cobalt(II) Complexes with Positive Axial and Large Rhombic Anisotropy. *Dalt. Trans.* **2019**, *48* (4), 1404−1417.
(26) Gómez-Coca, S.; Urtizberea, A.; Cremades, E.; Alonso, P. J.; Camón, A.; Ruiz, E.; Luis, F. Origin of Slow Magnetic Relaxation in Kramers Ions with Non-Uniaxial Anisotropy. *Nat. Commun.* **2014**, *5*, 1−8.
(27) Zadrozny, J. M.; Liu, J.; Piro, N. A.; Chang, C. J.; Hill, S.; Long, J. R. Slow Magnetic Relaxation in a Pseudotetrahedral Cobalt(II) Complex with Easy-Plane Anisotropy. *Chem. Commun.* **2012**, *48* (33), 3927.
(28) Boča, R.; Miklovič, J.; Titiš, J. Simple Mononuclear Cobalt(II) Complex: A Single-Molecule Magnet Showing Two Slow Relaxation Processes. *Inorg. Chem.* **2014**, *53* (5), 2367−2369.
(29) Vaidya, S.; Upadhyay, A.; Singh, S. K.; Gupta, T.; Tewary, S.; Langley, S. K.; Walsh, J. P. S.; Murray, K. S.; Rajaraman, G.; Shanmugam, M. A Synthetic Strategy for Switching the Single Ion Anisotropy in Tetrahedral Co(II) Complexes. *Chem. Commun.* **2015**, *51* (18), 3739−3742.
(30) Cao, D.-K.; Wei, R.-H.; Li, X.-X.; Gu, Y.-W. Multifunctional Mononuclear Bisthienylethene-Cobalt(II) Complexes: Structures, Slow Magnetic Relaxation and Photochromic Behavior. *Dalt. Trans.* **2015**, *44* (12), 5755−5762.
(31) Smolko, L.; Černák, J.; Dušek, M.; Miklovič, J.; Titiš, J.; Boča, R. Three Tetracoordinate Co(II) Complexes [Co(Biq)X2] (X = Cl, Br, I) with Easy-Plane Magnetic Anisotropy as Field-Induced Single-Molecule Magnets. *Dalt. Trans.* **2015**, *44* (40), 17565−17571.
(32) Bruno, R.; Vallejo, J.; Marino, N.; De Munno, G.; Krzystek, J.; Cano, J.; Pardo, E.; Armentano, D. Cytosine Nucleobase Ligand: A Suitable Choice for. Modulating Magnetic Anisotropy in Tetrahedrally Coordinated Mononuclear Co-II Compounds. *Inorg. Chem.* **2017**, *56* (4), 1857−1864.
(33) Świtlicka, A.; Machura, B.; Kruszynski, R.; Cano, J.; Toma, L. M.; Lloret, F.; Julve, M. The Influence of Pseudohalide Ligands on the SIM Behaviour of Four-Coordinate Benzylimidazole-Containing Cobalt(Ii) Complexes. *Dalton Trans.* **2018**, *47* (16). 5831.
(34) Buchholz, A.; Eseola, A. O.; Plass, W. Slow Magnetic Relaxation in Mononuclear Tetrahedral Cobalt(II) Complexes with 2-(1H-Imidazol-2-Yl)Phenol Based Ligands. *C. R. Chim.* **2012**, *15* (10), 929−936.
(35) Yang, F.; Zhou, Q.; Zhang, Y.; Zeng, G.; Li, G.; Shi, Z.; Wang, B.; Feng, S. Inspiration from Old Molecules: Field-Induced Slow Magnetic Relaxation in Three Air-Stable Tetrahedral Cobalt(II) Compounds. *Chem. Commun.* **2013**, *49* (46), 5289.
(36) Cao, D.-K.; Feng, J.-Q.; Ren, M.; Gu, Y.-W.; Song, Y.; Ward, M. D. A Mononuclear Cobalt(II)−Dithienylethene Complex Showing Slow Magnetic Relaxation and Photochromic Behavior. *Chem. Commun.* **2013**, *49* (78), 8863.
(37) Huang, W.; Liu, T.; Wu, D.; Cheng, J.; Ouyang, Z. W.; Duan, C. Field-Induced Slow Relaxation of Magnetization in a Tetrahedral Co(II) Complex with Easy Plane Anisotropy. *Dalt. Trans.* **2013**, *42* (43), 15326.
(38) Titiš, J.; Miklovič, J.; Boča, R. Magnetostructural Study of Tetracoordinate Cobalt(II) Complexes. *Inorg. Chem. Commun.* **2013**, *35*, 72−75.
(39) Zadrozny, J. M.; Telser, J.; Long, J. R. Slow Magnetic Relaxation in the Tetrahedral Cobalt(II) Complexes [Co(EPh)4]2-(EO, S, Se). *Polyhedron* **2013**, *64*, 209−217.
(40) Saber, M. R.; Dunbar, K. R. Ligands Effects on the Magnetic Anisotropy of Tetrahedral Cobalt Complexes. *Chem. Commun.* **2014**, *50* (82), 12266−12269.
(41) Fataftah, M. S.; Zadrozny, J. M.; Rogers, D. M.; Freedman, D. E. A Mononuclear Transition Metal Single-Molecule Magnet in a Nuclear Spin-Free Ligand Environment. *Inorg. Chem.* **2014**, *53* (19), 10716−10721.
(42) Habib, F.; Luca, O. R.; Vieru, V.; Shiddiq, M.; Korobkov, I.; Gorelsky, S. I.; Takase, M. K.; Chibotaru, L. F.; Hill, S.; Crabtree, R. H.; et al. Influence of the Ligand Field on Slow Magnetization Relaxation versus Spin Crossover in Mononuclear Cobalt Complexes. *Angew. Chem., Int. Ed.* **2013**, *52* (43), 11290−11293.
(43) Vallejo, J.; Pardo, E.; Viciano-Chumillas, M.; Castro, I.; Amoros, P.; Deniz, M.; Ruiz-Perez, C.; Yuste-Vivas, C.; Krzystek, J.; Julve, M.; et al. Reversible Solvatomagnetic Switching in a Single-Ion Magnet from an Entatic State. *Chem. Sci.* **2017**, *8* (5), 3694−3702.
(44) Nedelko, N.; Kornowicz, A.; Justyniak, I.; Aleshkevych, P.; Prochowicz, D.; Krupiński, P.; Dorosh, O.; Slawska-Waniewska, A.; Lewiński, J. Supramolecular Control over Molecular Magnetic Materials: γ-Cyclodextrin-Templated Grid of Cobalt(II) Single-Ion Magnets. *Inorg. Chem.* **2014**, *53* (24), 12870−12876.
(45) Piñero Cruz, D. M.; Woodruff, D. N.; Jeon, I.-R.; Bhowmick, I.; Secu, M.; Hillard, E. a.; Dechambenoit, P.; Clérac, R. Switching off the Single-Molecule Magnet Properties of the [CoII(Me6tren)-(OH2)]2+ Module by Complexation with Trans-[RuIII(Salen)(CN)-2]-. *New J. Chem.* **2014**, *38* (8), 3443.
(46) Colacio, E.; Ruiz, J.; Ruiz, E.; Cremades, E.; Krzystek, J.; Carretta, S.; Cano, J.; Guidi, T.; Wernsdorfer, W.; Brechin, E. K. Slow Magnetic Relaxation in a CoII-YIII Single-Ion Magnet with Positive Axial Zero-Field Splitting. *Angew. Chem., Int. Ed.* **2013**, *52* (35), 9130−9134.
(47) Chandrasekhar, V.; Dey, A.; Mota, A. J.; Colacio, E. Slow Magnetic Relaxation in Co(III)-Co(II) Mixed-Valence Dinuclear Complexes with a CoIIO5X (X = Cl, Br, NO3) Distorted-Octahedral Coordination Sphere. *Inorg. Chem.* **2013**, *52* (8), 4554.
(48) Wu, D.; Zhang, X.; Huang, P.; Huang, W.; Ruan, M.; Ouyang, Z. W. Tuning Transverse Anisotropy in CoIII-CoII-CoIII Mixed-Valence Complex toward Slow Magnetic Relaxation. *Inorg. Chem.* **2013**, *52* (19), 10976.
(49) Novikov, V. V.; Pavlov, A. A.; Nelyubina, Y. V.; Boulon, M.-E.; Varzatskii, O. A.; Voloshin, Y. Z.; Winpenny, R. E. P. A Trigonal

DOI: 10.1021/acs.inorgchem.9b01719
Inorg. Chem. 2019, 58, 15726−15740

Prismatic Mononuclear Cobalt(II) Complex Showing Single-Molecule Magnet Behavior. *J. Am. Chem. Soc.* **2015**, *137* (31), 9792−9795.
(50) Huang, X.-C.; Zhou, C.; Shao, D.; Wang, X.-Y. Field-Induced Slow Magnetic Relaxation in Cobalt(II) Compounds with Pentagonal Bipyramid Geometry. *Inorg. Chem.* **2014**, *53* (24), 12671−12673.
(51) Chen, L.; Chen, S.-Y.; Sun, Y.-C.; Guo, Y.-M.; Yu, L.; Chen, X.-T.; Wang, Z.; Ouyang, Z. W.; Song, Y.; Xue, Z.-L. Slow Magnetic Relaxation in Mononuclear Seven-Coordinate Cobalt(II) Complexes with Easy Plane Anisotropy. *Dalt. Trans.* **2015**, *44* (25), 11482−11490.
(52) Stoll, S.; Schweiger, A. Easy Spin, a Comprehensive Software Package for Spectral Simulation and Analysis in EPR. *J. Magn. Reson.* **2006**, *178* (1), 42−55.
(53) Angeli, C.; Cimiraglia, R.; Evangelisti, S.; Leininger, T.; Malrieu, J.-P. Introduction of N-Electron Valence States for Multireference Perturbation Theory. *J. Chem. Phys.* **2001**, *114* (23), 10252.
(54) Angeli, C.; Cimiraglia, R.; Malrieu, J.-P. N-Electron Valence State Perturbation Theory: A Fast Implementation of the Strongly Contracted Variant. *Chem. Phys. Lett.* **2001**, *350* (3−4), 297−305.
(55) Angeli, C.; Cimiraglia, R.; Malrieu, J.-P. N-Electron Valence State Perturbation Theory: A Spinless Formulation and an Efficient Implementation of the Strongly Contracted and of the Partially Contracted Variants. *J. Chem. Phys.* **2002**, *117* (20), 9138.
(56) Neese, F. The ORCA Program System. *Wires Comput. Mol. Sci.* **2012**, *2* (1), 73−78.
(57) Schafer, A.; Horn, H.; Ahlrichs, R. Fully Optimized Contracted Gaussian Basis Sets for Atoms Li to Kr. *J. Chem. Phys.* **1992**, *97* (4), 2571.
(58) Schafer, A.; Huber, C.; Ahlrichs, R. Fully Optimized Contracted Gaussian Basis Sets of Triple Zeta Valence Quality for Atoms Li to Kr. *J. Chem. Phys.* **1994**, *100* (8), 5829.
(59) Eichkorn, K.; Weigend, F.; Treutler, O.; Ahlrichs, R. Auxiliary Basis Sets for Main Row Atoms and Transition Metals and Their Use to Approximate Coulomb Potentials. *Theor. Chem. Acc.* **1997**, *97* (1−4), 119−124.
(60) Eichkorn, K.; Treutler, O.; Öhm, H.; Häser, M.; Ahlrichs, R. Auxiliary Basis Sets to Approximate Coulomb Potentials. *Chem. Phys. Lett.* **1995**, *240* (4), 283−289.
(61) Vancoillie, S.; Chalupský, J.; Ryde, U.; Solomon, E. I.; Pierloot, K.; Neese, F.; Rulíšek, L. Multireference Ab Initio Calculations of g Tensors for Trinuclear Copper Clusters in Multicopper Oxidases. *J. Phys. Chem. B* **2010**, *114* (22), 7692−7702.
(62) *Gaussian-09*; Frisch, M. J.; Trucks, G. W.; Schlegel, H. B.; Scuseria, G. E.; Robb, M. A.; Cheeseman, J. R.; Scalmani, G.; Barone, V.; Mennucci, B.; et al. Gaussian 09 (Revision B.1); Gaussian, Inc.: Wallingford, CT, 2009.
(63) Lee, C.; Yang, W.; Parr, R. G. Development of the Colle-Salvetti Correlation-Energy Formula into a Functional of the Electron Density. *Phys. Rev. B: Condens. Matter Mater. Phys.* **1988**, *37* (2), 785−789.
(64) Becke, A. D. Density-Functional Thermochemistry. III. The Role of Exact Exchange. *J. Chem. Phys.* **1993**, *98* (7), 5648−5652.
(65) Becke, A. D. Density-Functional Exchange-Energy Approximation with Correct Asymptotic Behavior. *Phys. Rev. A: At., Mol., Opt. Phys.* **1988**, *38* (6), 3098−3100.
(66) Yanai, T.; Tew, D. P.; Handy, N. C. A New Hybrid Exchange-Correlation Functional Using the Coulomb-Attenuating Method (CAM-B3LYP). *Chem. Phys. Lett.* **2004**, *393* (1−3), 51−57.
(67) Ruiz, E.; Rodríguez-Fortea, A.; Cano, J.; Alvarez, S.; Alemany, P. About the Calculation of Exchange Coupling Constants in Polynuclear Transition Metal Complexes. *J. Comput. Chem.* **2003**, *24* (8), 982−989.
(68) Ruiz, E.; Cano, J.; Alvarez, S.; Alemany, P. Broken Symmetry Approach to Calculation of Exchange Coupling Constants for Homobinuclear and Heterobinuclear Transition Metal Complexes. *J. Comput. Chem.* **1999**, *20* (13), 1391−1400.
(69) Ruiz, E.; Cano, J.; Alvarez, S.; Alemany, P. Magnetic Coupling in End-on Azido-Bridged Transition Metal Complexes: A Density Functional Study. *J. Am. Chem. Soc.* **1998**, *120* (43), 11122−11129.
(70) Tomasi, J.; Mennucci, B.; Cancès, E. The IEF Version of the PCM Solvation Method: An Overview of a New Method Addressed to Study Molecular Solutes at the QM Ab Initio Level. *J. Mol. Struct.: THEOCHEM* **1999**, *464* (1−3), 211−226.
(71) *SAINT*, Version 6.45; Bruker Analytical X-ray Systems: Madison, WI, 2003.
(72) Sheldrick, G. M. *SADABS Program for Absorption Correction*, version 2. 1; Analytical X-Ray Systems: Madison, WI, 2003.
(73) Sheldrick, G. M. Crystal Structure Refinement with SHELXL. *Acta Crystallogr., Sect. C: Struct. Chem.* **2015**, *71* (1), 3−8.
(74) Spek, A. L. Pl. *Acta Crystallogr., Sect. D: Biol. Crystallogr.* **2009**, *65*, 148.
(75) Palmer, D. *CrystalMaker*; Cambridge University Technical Services: Cambridge, 1996.
(76) Deacon, G. Relationships between the Carbon-Oxygen Stretching Frequencies of Carboxylato Complexes and the Type of Carboxylate Coordination. *Coord. Chem. Rev.* **1980**, *33* (3), 227−250.
(77) Nakamoto, K. *Infrared and Raman Spectra of Inorganic and Coordination Compounds*; John Wiley & Sons, Inc.: Hoboken, NJ, USA, 2008. .
(78) Rosenthal, M. R. The Myth of the Non-Coordinating Anion. *J. Chem. Educ.* **1973**, *50* (5), 331.
(79) Baca, S. G.; Filippova, I. G.; Ambrus, C.; Gdaniec, M.; Simonov, Y. A.; Gerbeleu, N.; Gherco, O. A.; Decurtins, S. From Mono- and Dinuclear to Polynuclear Cobalt(II) and Cobalt(III) Coordination Compounds Based on o-Phthalic Acid and 2,2'-Bipyridine: Synthesis, Crystal Structures, and Properties. *Eur. J. Inorg. Chem.* **2005**, *2005* (15), 3118−3130.
(80) Cano, J.; De Munno, G.; Luis Sanz, J.; Ruiz, R.; Faus, J.; Lloret, F.; Julve, M.; Caneschi, A. Ability of Terephthalate (Ta) to Mediate Exchange Coupling in Ta-Bridged Copper(II), Nickel(II), Cobalt(II) and Manganese(II) Dinuclear Complexes. *J. Chem. Soc., Dalton Trans.* **1997**, No. 11, 1915−1924.
(81) Llunell, M.; Casanova, D.; Cirera, J.; Alemany, P.; Alvarez, S. *SHAPE v1.1b*; Barcelona, 2013.
(82) Moseley, D. H.; Stavretis, S. E.; Thirunavukkuarasu, K.; Ozerov, M.; Cheng, Y.; Daemen, L. L.; Ludwig, J.; Lu, Z.; Smirnov, D.; Brown, C. M.; et al. Spin−Phonon Couplings in Transition Metal Complexes with Slow Magnetic Relaxation. *Nat. Commun.* **2018**, *9* (1), 2572.
(83) Krzystek, J.; Zvyagin, S. A.; Ozarowski, A.; Trofimenko, S.; Telser, J. Tunable-Frequency High-Field Electron Paramagnetic Resonance. *J. Magn. Reson.* **2006**, *178* (2), 174−183.
(84) Lloret, F.; Julve, M.; Cano, J.; Ruiz-García, R.; Pardo, E. Magnetic Properties of Six-Coordinated High-Spin Cobalt(II) Complexes: Theoretical Background and Its Application. *Inorg. Chim. Acta* **2008**, *361* (12−13), 3432.
(85) Cano, J. *VPMAG Package*; University of Valencia: Valencia, Spain, 2003.
(86) Lines, M. E. Orbital Angular Momentum in the Theory of Paramagnetic Clusters. *J. Chem. Phys.* **1971**, *55* (6), 2977−2984.
(87) Gingsberg, A. P. Magnetic Exchange in Transition Metal Complexes vi: Aspects of Exchange Coupling in Magnetic Cluster Complexes. *Inorg. Chim. Acta, Rev.* **1971**, *5*, 45−68.
(88) Palii, A. V.; Tsukerblat, B. S.; Coronado, E.; Clemente-Juan, J. M.; Borrás-Almenar, J. J. Microscopic Approach to the Pseudo-Spin-1/2 Hamiltonian for Kramers Doublets in Exchange Coupled Co(II) Pairs. *Inorg. Chem.* **2003**, *42* (7), 2455−2458.
(89) Cole, K. S.; Cole, R. H. Dispersion and Absorption in Dielectrics I. Alternating Current Characteristics. *J. Chem. Phys.* **1941**, *9* (4), 341.
(90) Zhang, J.; Li, J.; Yang, L.; Yuan, C.; Zhang, Y.-Q.; Song, Y. Magnetic Anisotropy from Trigonal Prismatic to Trigonal Antiprismatic Co(II) Complexes: Experimental Observation and Theoretical Prediction. *Inorg. Chem.* **2018**, *57* (7), 3903−3912.
(91) Feng, X.; Liu, J.; Harris, T. D.; Hill, S.; Long, J. R. Slow Magnetic Relaxation Induced by a Large Transverse Zero-Field

DOI: 10.1021/acs.inorgchem.9b01719
Inorg. Chem. 2019, 58, 15726−15740

Splitting in a MnIIReIV(CN)2 Single-Chain Magnet. *J. Am. Chem. Soc.* **2012**, *134* (17), 7521−7529.
(92) Atzori, M.; Tesi, L.; Benci, S.; Lunghi, A.; Righini, R.; Taschin, A.; Torre, R.; Sorace, L.; Sessoli, R. Spin Dynamics and Low Energy Vibrations: Insights from Vanadyl-Based Potential Molecular Qubits. *J. Am. Chem. Soc.* **2017**, *139* (12), 4338−4341.
(93) Lunghi, A.; Totti, F.; Sessoli, R.; Sanvito, S. The Role of Anharmonic Phonons in Under-Barrier Spin Relaxation of Single Molecule Magnets. *Nat. Commun.* **2017**, *8*, 14620.
(94) Escalera-Moreno, L.; Suaud, N.; Gaita-Ariño, A.; Coronado, E. Determining Key Local Vibrations in the Relaxation of Molecular Spin Qubits and Single-Molecule Magnets. *J. Phys. Chem. Lett.* **2017**, *8* (7), 1695−1700.

DOI: 10.1021/acs.inorgchem.9b01719
Inorg. Chem. 2019, 58, 15726−15740